New Advances of the P-SBAS Approach for an Efficient Parallel Processing of Large Volumes of Full-Resolution Multi-Temporal DInSAR Interferograms

Manuela Bonano, Pasquale Striano, Muhammad Yasir, Sabatino Buonanno, Francesco Casu, Claudio De Luca, Adele Fusco, Yenni Lorena Belen Roa, Ivana Zinno, Maria Virelli, Michele Manunta, and Riccardo Lanari, *Fellow, IEEE*

***Abstract*— This paper presents an innovative, parallel implementation of the Small BAseline Subset (SBAS) approach to automatically and efficiently process large volumes of multi-temporal Differential Synthetic Aperture Radar (SAR) Interferometry (DInSAR) interferograms generated at the native full spatial resolution of the SAR images. The starting point of the developed Full-Resolution Parallel-SBAS (FR P-SBAS) technique involves some algorithmic extensions for improving the quality of the DInSAR time series to effectively analyze extended deformations and localized displacement phenomena affecting single buildings and infrastructures. A key point of the work is the efficient and scalable FR P-SBAS processing chain implementation, focused on exploiting GPU architectures. The presented scalability analysis demonstrates the GPU capability to efficiently generate full-resolution displacement time series starting from large DInSAR datasets. Moreover, the processing solution easily allows us to deal with SAR data acquired through the Stripmap and TOPS modes. To assess the quality of the generated DInSAR products, an extensive experimental analysis is also shown, based on long sequences of X-Band COSMO-SkyMed Stripmap and C-Band Sentinel-1 TOPS acquisitions relevant to the Campi Flegrei Caldera (Southern Italy), which is monitored through a dense GNSS network. The presented results demonstrate the effectiveness of the FR P-SBAS processing chain in retrieving multi-frequency and multi-platform displacement time series at the full spatial resolution with sub-centimetric accuracy and in very short time frames, from a few hours for the COSMO-SkyMed datasets up to some tens of hours for the Sentinel-1 one.**

***Index Terms*— DInSAR, P-SBAS, Full-resolution displacement time series, GPU, COSMO-SkyMed, Sentinel-1, GNSS**

I. INTRODUCTION

THE Earth Observation (EO) scenario has been experiencing a revolution thanks to the huge volume of remote sensing data nowadays available. In particular, the widespread availability of Synthetic Aperture Radar (SAR) data systematically acquired during the last three decades by several space-borne sensors operating with different spatial resolutions, footprint extensions, revisit times, and bandwidths (typically X-, C-, and L-band), has promoted the development of several EO methodologies. Among these, the Differential SAR Interferometry (DInSAR) technique [1][2] may provide valuable information on the surface displacements, projected into the radar Line of Sight (LOS), affecting wide areas, which can be investigated with rather limited costs by exploiting the phase difference (interferogram) between pairs of complex-value SAR images acquired at different times (the temporal separation is usually referred to as temporal baseline) and from relatively close flight tracks (the orbital separation is typically known as spatial baseline). Originally designed and applied to investigate single deformation episodes, such as seismic events and volcanic unrests [3][4], the DInSAR methodology has evolved toward the study of the temporal evolution of the detected displacements thanks to the development of multi-temporal (also referred to as advanced) DInSAR techniques [5]-[11]. Such approaches, which are based on the inversion of a large number of multi-temporal differential interferograms relevant to an area of interest, provide helpful information on the spatial and temporal characteristics of the detected deformation, through the generation of displacement time series. Among several multi-temporal DInSAR algorithms, the

This study has been partly funded by the Italian Civil Protection Department (DPC) in the frame of the IREA-DPC (2022-2024) agreement, although it does not necessarily represent the DPC's official opinion and policies. This research was also partially funded by the European Union -Next Generation EU (PNRR-M4C2) through the following projects: CN-MOST (CN00000023); ICSC - CN-HPC (CN00000013); MEET IR (IR0000025); GeoSciences IR (IR0000037). This research was also supported by the GRINT (PIR01_00013) and IBiSCo (PIR01_00011) projects, funded by the National Operational Programme Infrastructures and Networks 2014/2020 of the Italian Ministry of Infrastructure and Transports. *(Corresponding author: Michele Manunta).*

Manuela Bonano, Pasquale Striano, Muhammad Yasir, Sabatino Buonanno, Claudio De Luca, Adele Fusco, Yenni Lorena Belen Roa, Ivana Zinno, Michele Manunta, and Riccardo Lanari are with Istituto per il Rilevamento Elettromagnetico dell'Ambiente (IREA), Consiglio Nazionale delle Ricerche (CNR), 80124, Napoli, Italy (e-mail: bonano.m, striano.p, yasir.m, buonanno.s, deluca.c, fusco.a, roa.y, zinno.i, manunta.m, lanari.r@irea.cnr.it).

Francesco Casu is with Istituto per il Rilevamento Elettromagnetico dell'Ambiente (IREA), Consiglio Nazionale delle Ricerche (CNR), 20133, Milano, Italy (e-mail: casu.f@irea.cnr.it).

Maria Virelli is with the Italian Space Agency (ASI), 00133, Roma, Italy (e-mail: maria.virelli@asi.it).

Color versions of one or more of the figures in this article are available online at http://ieeexplore.ieee.org

Small BAseline Subset (SBAS) technique [6] generates LOS-projected displacement time series and the corresponding velocity maps by properly exploiting SAR data pairs characterized by small spatial and/or temporal baselines, thus allowing us to mitigate the noise (decorrelation phenomena) affecting the computed interferograms and to maximize the number of detected coherent points [12]. The SBAS approach has proven effective in detecting and monitoring displacement signals with millimeter accuracy in several natural and anthropic hazard scenarios, such as volcanoes, tectonics, landslides, and anthropogenic and hydrogeological risk contexts [13]-[26].

Furthermore, we remark that the exploitation of both the triangular coherence factor [27] and appropriate filtering methods [28] avoids the presence, as discussed in [29], of what has been recently reported as "bias effects" that may affect multi-look interferograms based DInSAR products [30]. We further underline that one key point of the SBAS approach consists in its capability to generate displacement time series (and the corresponding mean velocity maps) at two different spatial resolution scales, referred hereinafter to as regional and local scales, respectively [8][31][32]. This is accomplished by dealing with both multi-look interferograms (the regional scale or medium resolution analysis is typically carried out with a spatial resolution in the range 20-100 m) and full-resolution interferograms (the local scale or full-resolution analysis is performed with a spatial resolution in the 1-20 m range). Such a peculiarity has deeply contributed to the wide dissemination of the SBAS approach within the Solid Earth scientific community, as it is particularly suitable for a wide range of applications, from civil protection scenarios (e.g., volcanic eruptions, seismic events, and landslides) to anthropogenic contexts (e.g., extended urban areas, archaeological and historical sites, oil-gas extraction areas, structures and transport infrastructures, and mines).

However, due to the rapid evolution of the multi-temporal DInSAR scenario, which demands the processing of massive volumes of interferometric datasets composed of hundreds of SAR images, the need to develop effective solutions to manage and process such a huge data flow became urgent. In this framework, a successful solution has already been adopted for the regional scale interferometric analysis through the Parallel SBAS (P-SBAS) processing chain [27][33]. It consists of a parallel implementation of the medium resolution SBAS workflow, based on the exploitation of distributed High Performance Computing (HPC) e-infrastructures, also accessible through Cloud Computing environments [34], as well as multi-node, multi-core, and multi-thread parallel computing strategies, aimed to the automatic and unsupervised processing of large SAR data volumes, guaranteeing high scalability performance [35]-[37].

Unfortunately, the dimension of the full-resolution SBAS datasets, which nowadays may comprise hundreds to thousands of DInSAR interferometric SAR data pairs and hundreds of millions of pixels to be processed at the full spatial resolution of the sensors, is about two orders of magnitude greater than the typical size of the corresponding medium resolution ones. If addressed with a conventional implementation approach, this may represent a severe bottleneck regarding the overall computing time and data load. Accordingly, to speed up the overall full-resolution SBAS processing chain at reasonable time frames and to achieve high efficiency in terms of scalability and computing performance, the development of more advanced, multi-temporal interferometric techniques for maximizing the information related to the huge amount of available DInSAR data, as well as the implementation of efficient parallel computing solutions based on up-to-date distributed HPC e-infrastructures, are recommended and foreseen.

In this context, a very effective solution is represented by the one based on properly exploiting an HPC architecture consisting of multi-core (CPU) and many-core Graphical Processing Unit (GPU) devices. Indeed, the CPUs comprise a few cores (i.e., typically some tens) optimized to speed up the sequential processing. In contrast, the GPUs have an intrinsically parallel architecture consisting of thousands of smaller but highly efficient cores, designed for handling multiple tasks simultaneously, such as those related to deep learning, analytics, and data mining. We further remark that, although the GPUs were initially designed to deal with graphic applications, they have recently been broadly used with any application software where single instructions are carried out on multiple data, usually called SIMD (Single Instruction, Multiple Data) approaches [38][39].

While the multi-core CPU-based strategy is largely exploited to implement efficient DInSAR processing chains [36][40], the use of GPUs seems to be rather underexploited. Indeed, although these devices are currently easily accessible also in Cloud Computing environments and their relatively high cost is decreasing, there are still some technological drawbacks related to a lack of their exploitation: (*i*) GPU programming codes are more complex than the corresponding CPU ones, (*ii*) the code sources developed for CPUs cannot be easily adapted to run on GPU devices, (*iii*) GPUs are suitable to carry out simple computations on multiple data in a very effective way, thus demanding ad-hoc algorithmic implementation, and (*iv*) the efficient use of GPUs can force towards the exploitation of algorithmic solutions that may have a substantial impact even on the procedures that do not benefit from GPUs.

However, as GPU performance continues to grow, providing a real advantage (in terms of efficiency and computing time) for various application software, their use has also started spreading in the SAR and DInSAR communities [38][41][43].

In this work, we present new advances in the full-resolution SBAS algorithm to effectively retrieve the displacement time series and the corresponding mean velocity maps of the investigated areas. In particular, the developed modifications aim to improve the quality of the generated displacement time series to effectively analyze extended deformations and localized displacement phenomena, like those affecting single buildings and/or infrastructures. Moreover, the presented algorithmic solution also encompasses some modifications able

to deal with multi-platform SAR signals, thus allowing to process data acquired through both the Stripmap and the TOPS [44] modes, the latter characterizing the Interferometric Wide Swath (IWS) acquisition capability of the Sentinel-1 (S-1) constellation [45].

A key point of this work is the parallel implementation of the full-resolution SBAS processing chain, based on the effective exploitation of innovative hardware and software parallel technologies, mainly using GPUs. Starting from the first activities presented by [46] and [47], we focus here on the more computationally intensive blocks of the full-resolution SBAS workflow, where the parallelization strategies based on multi-core/multi-node CPU programming solutions are not sufficiently efficient in terms of processing time and data load balance. Accordingly, to speed up the full-resolution P-SBAS processing chain, as anticipated, we extensively exploit up-to-date HPC infrastructures equipped with GPU devices, able to effectively manage and process vast amounts of full-resolution DInSAR data stacks in short time frames, guaranteeing high efficiency in terms of computational load and scalability performance.

Finally, an extensive analysis of the implemented solution performance, which investigates both the DInSAR data processing efficiency and the quality of the generated products, is presented.

The paper is organized as follows. In Section II, the primary rationale of the two-scale SBAS processing chain is summarized. Section III presents the main algorithmic advances introduced within the full-resolution SBAS approach, which also allows for dealing with both Stripmap and TOPS SAR data. Section IV describes the full-resolution parallel SBAS processing chain implementation, with a specific focus on the adopted parallelization strategy, which makes use of hardware and software parallel technologies mostly based on GPUs. Section V aims to present a scalability analysis of the implemented algorithmic solution, which is carried out by investigating the performance of the parallel approach concerning the available computing power. In Section VI, the results achieved by processing extensive archives of full-resolution X-band first- and second-generation COSMO-SkyMed data, as well as of full-resolution C-band Sentinel-1 images relevant to the city of Naples (Italy), are presented. Finally, Section VII provides some conclusive remarks.

II. The Two-scale SBAS-DInSAR Approach

This Section summarizes the rationale of the two-scale SBAS-DInSAR algorithm, originally designed to analyze the space/time characteristics of the investigated displacement phenomena at two different spatial resolution scales: regional and local. As already said, this capability makes the two-scale SBAS approach quite flexible and suitable to be adopted in many applications, from civil protection scenarios to anthropogenic contexts. In particular, the two-scale SBAS approach follows the lines of the algorithm initially presented in [8], see Fig. 1, and subsequently extended to multi-sensor analyses[32]. The rationale of the approach consists of two

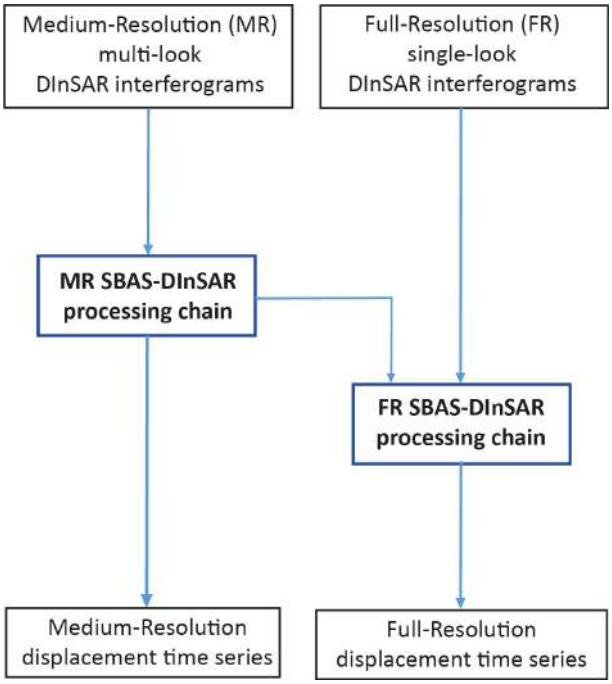

Fig. 1. Conceptual scheme of the two-scale SBAS-DInSAR approach.

subsequent pipelines, hereinafter referred to as medium-resolution (MR) and full-resolution (FR) SBAS processing chains, which generate regional and local scale DInSAR products, respectively, mainly represented by displacement time series (and the corresponding mean velocity maps).

The MR SBAS-DInSAR processing chain was initially described by [6], and for what concerns its parallel algorithmic implementations, it is detailed in [33] for the Stripmap mode and in [27] for the TOPS one. This implementation starts from a list of SLC images (note that raw data could also be considered, but they are not always available), co-registered on a reference SAR image geometry and coupled according to a selection of small (temporal and/or perpendicular) baseline interferometric SAR data pairs[6] [48], to compute a redundant number of multi-look interferograms. The small baseline interferogram sequence is then unwrapped [48] and subsequently "inverted" through the Singular Value Decomposition (SVD) method [49] to retrieve the MR displacement components and to identify the Atmospheric Phase Screen (APS) signals, as well as those caused by possible orbital inaccuracies [50].

The FR SBAS processing chain, which will be thoroughly discussed in the following, is aimed at generating the DInSAR products at the full spatial resolution scale by exploiting both the single-look differential interferograms and the MR interferometric results derived from the multi-look interferograms involved in the regional scale MR SBAS analysis. Note that, for the sake of completeness and to avoid any confusion with the used glossary, throughout the text the medium-resolution (MR), low-pass (LP), or multi-look (ML) terms refer to the regional scale DInSAR products. In contrast,

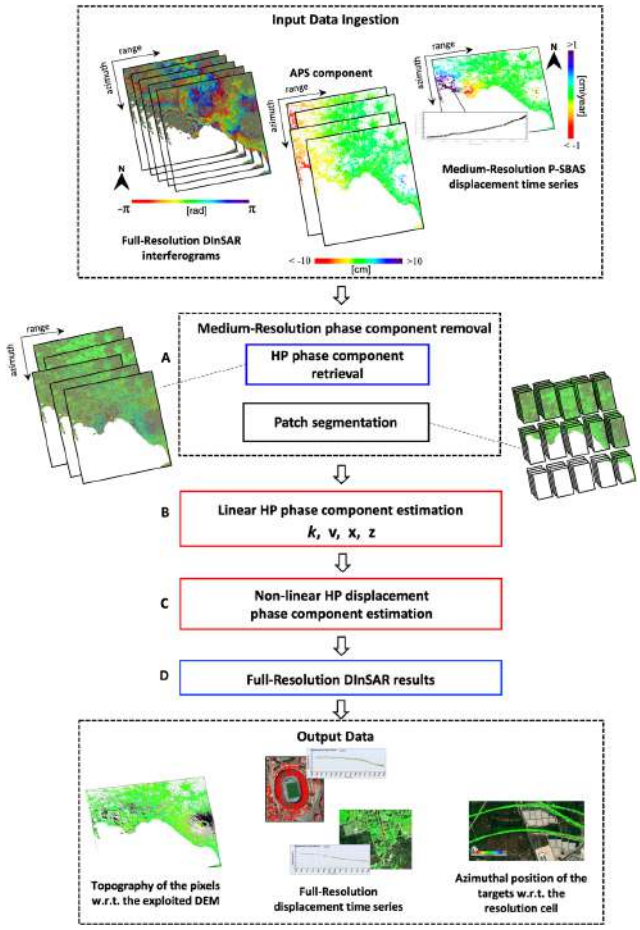

Fig. 2. Simplified block diagram of the Full-Resolution SBAS-DInSAR algorithm. The blue and red blocks represent the processing steps executed in parallel that are implemented through CPU cores and GPU devices, respectively; the black block stands for a sequentially executed processing step.

the Single-Look (SL), full-resolution (FR), high-resolution (HR), and high-pass (HP) terms are used to specify the high spatial frequency information deriving from the full-resolution interferograms.

A detailed description of the MR SBAS algorithm is outside the scope of this work because, as said, it can be found in [6][27][33]. Accordingly, in the following analysis, we focus on the full-resolution SBAS processing chain, describing the main algorithmic advances, preliminarily shown in [46] and [47].

III. The FR SBAS-DInSAR Algorithm

This Section is dedicated to describing the main steps of the implemented FR SBAS-DInSAR processing chain, as well as including a discussion about their mathematical framework. It is also worth remarking that the developed processing pipeline has been originally conceived to deal with multi-platform full-resolution SAR data acquired through the Stripmap mode, such as those related to the Italian X-band COSMO-SkyMed (CSK) constellation; however, as shown in the following, it can be easily adapted to process data collected through the ScanSAR and the TOPS mode, the latter used to acquire the Sentinel- 1 (IWS) SAR data.

Let us start this discussion by focusing on the block diagram of the FR SBAS-DInSAR processing chain, which consists of four main steps, as shown in Fig. 2. In particular, the pipeline starts with the ingestion of the input data, which is made of:

1) the whole sequence of FR (i.e., single-look) DInSAR interferograms, made of *M* interferometric pairs generated from coupling the available *N* SAR images;
2) the regional scale DInSAR products for each coherent multi-look pixel of the investigated area, consisting mainly of the MR displacement time series and the estimated Atmospheric Phase Screen components[1], obtained as output of the MR SBAS approach.

For each investigated pixel, the expression of the generic *i-th* full-resolution DInSAR interferogram, say $\Delta\phi_i^{FR}$, is the following [32]:

$$\Delta\phi_i^{FR} = \langle \frac{4\pi}{\lambda}\frac{b_i^{\perp}}{r\cdot\sin(\theta)}\cdot z + \frac{2\pi}{v_s}\Delta\xi_i\cdot x + \frac{4\pi}{\lambda}(d_i^{LP} + d_i^{HP}) + \Delta\phi_i^{ATM} + \Delta\phi_i^{noise}\rangle_{2\pi} \quad \forall i = 0,..,M-1 \tag{1}$$

wherein M represents the number of exploited interferograms, $\langle\cdot\rangle_{2\pi}$ represents the wrapping operator, λ is the radar wavelength, r is the sensor-to-target distance, θ is the incidence angle, $b_i^{\perp}$ represents the perpendicular baseline component, z is the topography of the target w.r.t. the exploited DEM, v_s is the platform velocity, $\Delta\xi_i$ stands for the Doppler Centroid (DC) difference between the two SAR acquisitions of the *i-th* interferometric pair and x takes into account the relative azimuthal position of the imaged targets w.r.t. the center of the resolution cell [32]. Moreover, d_i^{LP} and d_i^{HP} are the LP and HP components of the Line of Sight (LOS) projection of the displacements, respectively. Finally, the last two terms in (1) represent the phase components due to the different atmospheric conditions between the primary and the secondary acquisitions ($\Delta\phi_i^{ATM}$) and to the noise ($\Delta\phi_i^{noise}$) associated with the *i-th* interferogram, respectively.

Following the input data ingestion, the algorithm implements in Step A the MR phase components removal operation by applying, for each pixel in the full resolution grid of the DInSAR interferograms, the modulo-2π subtraction of the

[1] Note that further MR phase components can be accounted for, as for possible orbital inaccuracies, introducing, at the first order, ramps in the interferograms [50].

previously mentioned regional scale SBAS products from the single-look interferometric sequence. Such an operation allows retrieving, on a pixel basis, the residual HP interferometric phase component, say $\Delta\phi_i^{HP}$, whose expression for the generic *i-th* HP interferogram can be written as follows [46]:

$$\begin{aligned}\Delta\phi_i^{HP} &= \langle \Delta\phi_i^{FR} - \left(\Delta\phi_i^{ATM} + \frac{4\pi}{\lambda} d_i^{LP}\right)\rangle_{2\pi} \\ &= \langle \frac{4\pi}{\lambda}\frac{b_i^{\perp}}{r\cdot\sin(\theta)}\cdot z + \frac{2\pi}{v_s}\Delta\xi_i \cdot x \\ &+ \frac{4\pi}{\lambda} d_i^{HP} + \Delta\phi_i^{noise}\rangle_{2\pi} \\ &\forall i = 0,.,M-1\end{aligned} \tag{2}$$

Note that we expand in (2) the HP displacement term d_i^{HP} by decoupling it into a linear (with respect to time) $\Delta t_i \cdot v$ and a non-linear, say d_i^{nl}, HP components [8], wherein Δt_i and v are the temporal baseline of the *i-th* interferogram and the mean velocity of the HP displacement component, respectively. Moreover, if we focus on the temporally coherent pixels only, i.e., on the Persistent Scatterers (PS) [51][52], it is possible to consider negligible the noise term $\Delta\phi_i^{noise}$ in (2) without tampering with the mathematical framework. Accordingly, the expression in (2) can be re-written as follows [32][46]:

$$\begin{aligned}\Delta\phi_i^{HP} &= \langle \frac{4\pi}{\lambda}\frac{b_i^{\perp}}{r\cdot\sin(\theta)}\cdot z + \frac{2\pi}{v_s}\Delta\xi_i \cdot x + \frac{4\pi}{\lambda}\Delta t_i \cdot v \\ &+ \frac{4\pi}{\lambda} d_i^{nl}\rangle_{2\pi} \qquad \forall i = 0,..,M-1\end{aligned} \tag{3}$$

The residual HP interferometric phase component (3) is then used for the estimation, within Step B (see Fig. 2), of the "linear phase terms", i.e., the topography z, the azimuthal position x and the mean displacement velocity v. Such an estimation is implemented through the maximization of the temporal coherence factor [8][32]:

$$\gamma = \frac{1}{M}\left|\sum_{i=0}^{M-1} e^{j\left(\Delta\phi_i^{HP} - \Delta\phi_i^{model}\right)}\right| \qquad \forall i = 0,\dots M-1 \tag{4}$$

with

$$\Delta\phi_i^{model} = \frac{4\pi}{\lambda}\frac{b_i^{\perp}}{r\cdot\sin(\theta)}\cdot z + \frac{2\pi}{v_s}\Delta\xi_i \cdot x + \frac{4\pi}{\lambda}\Delta t_i \cdot v \tag{5}$$

Such a maximization procedure allows for identifying a set of coherent pixels with a value greater than a previously selected threshold. Note also that the estimation of the azimuthal position x is strictly correlated with the presence of adequate Doppler Centroid differences $\Delta\xi$ between the SAR images of the selected interferometric data pairs. Thus, it can be carried out when dealing with SAR sensors having such a characteristic (e.g., for ERS-2 during the gyroscope failure event [53] and for COSMO-SkyMed [47]).

It is also worth highlighting that the expression of the residual HP interferometric phase component in (3) can be further tailored according to the exploited SAR sensors. In particular, it may encompass additional terms not included in the original version of the FR SBAS-DInSAR approach [8][32], which may improve the characterization of the HP displacement component and, thus, enhance the retrieval of the overall displacements. This is, for instance, the case of a possible deformation component due to the material thermal dilation, which can be relevant in presence of metallic infrastructures and buildings, as well as in the reinforced concrete-based built-up environment. Considering, for instance, the high sensitivity of the X-band SAR data, the dilation of the material due to the temperature changes could cause significant seasonal variations in DInSAR displacement time series [55]-[60]. Hence, it may be crucial to also incorporate the thermal dilation factor in (3) and (5), to increase the reliability of the detected displacements affecting civil infrastructures. It is worth noting that the phase contribution relevant to the thermal effect can be correlated with the daily temperature records of the investigated area [61] and can be then reasonably expressed as a linear function with respect to the temperature variation between the primary and secondary acquisitions generating the *i-th* interferogram [62]. Accordingly, by introducing an additional phase component within the HP term, (3) can be rewritten as follows [46]:

$$\begin{aligned}\Delta\phi_i^{HP} &= \langle \frac{4\pi}{\lambda}\frac{b_i^{\perp}}{r\cdot\sin(\theta)}\cdot z + \frac{2\pi}{v_s}\Delta\xi_i \cdot x + \frac{4\pi}{\lambda}\Delta t_i \cdot v \\ &+ \frac{4\pi}{\lambda}\Delta Temp_i \cdot k + \frac{4\pi}{\lambda} d_i^{nl\_res}\rangle_{2\pi} \\ &\forall i = 0,\dots,M-1\end{aligned} \tag{6}$$

wherein k and $\Delta Temp_i$ represent the thermal dilation coefficient of the target and the differences of the temperatures associated with the primary and secondary time frames, respectively. Moreover, the term $d_i^{nl\_res}$ represents the residual non-linear HP displacement component. Hereinafter, throughout the paper we consider (6) as for the mathematical formulation of the residual HP phase component. Accordingly, the model described in (5), by considering (6), can be finally rewritten as follows:

$$\begin{aligned}\Delta\phi_i^{model} &= \frac{4\pi}{\lambda}\frac{b_i^{\perp}}{r\cdot\sin(\theta)}\cdot z + \frac{2\pi}{v_s}\Delta\xi_i \cdot x + \frac{4\pi}{\lambda}\Delta t_i \cdot v \\ &+ \frac{4\pi}{\lambda}\Delta Temp_i \cdot k\end{aligned} \tag{7}$$

We remark that Step B in Fig. 2 implements, on a pixel basis, the phase unwrapping operations over the residual HP phase components, performed through the estimation of the "linear" HP phase terms in (7), i.e., the topography z, the displacement

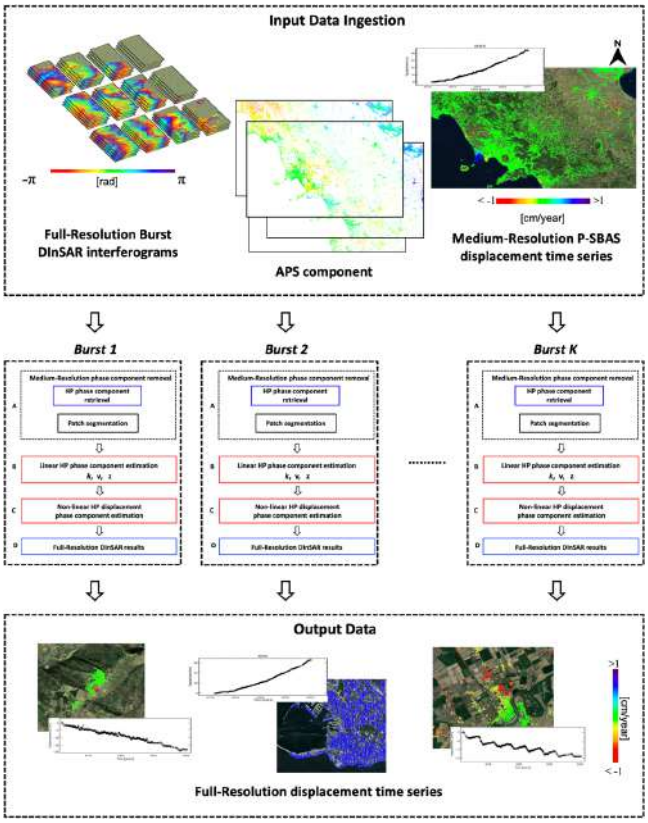

Fig. 3. Conceptual scheme of the FR SBAS-DInSAR processing chain dealing with the burst structure of the SAR data acquired through the TOPS (or ScanSAR) mode.

velocity v, the thermal dilation coefficient k and, whenever possible, the azimuthal position x.

Once the "linear" phase components in (7) are correctly estimated through the maximization of the temporal coherence in (4) (the operation carried out in Step B of Fig. 2), they are modulo-2π subtracted from the HP interferometric phase term $\Delta\phi_i^{HP}$ in (6), thus allowing to retrieve the residual non-linear HP displacement term that, for the generic *i-th* HP interferogram, can be expressed as follows:

$$\langle \Delta\phi_i^{HP} - \Delta\phi_i^{model} \rangle_{2\pi} = \frac{4\pi}{\lambda} d_i^{nl\_res} \tag{8}$$

For each coherent pixel, the inversion of the system in (8) aimed to correctly estimate the non-linear HP displacement terms is carried out by applying the SVD or Least Square methods [49] according to the conventional SBAS inversion strategy [8]. Such a procedure is implemented in Step C of the block diagram in Fig. 2. Note that this operation does not require any additional phase unwrapping operation on the residual non-linear term, since the investigated signals can be safely assumed within $[-\pi, \pi[$ interval.

Lastly, the generation of the overall FR displacement products is accomplished in Step D of Fig. 2, where the achieved HP linear (i.e., the mean velocity and thermal dilation factors associated with single structures) and the non-linear displacement components are properly added up to the MR measurements to retrieve the overall full-resolution displacement time series. It is worth noting that, besides the retrieved information (FR displacement time series), the FR SBAS processing chain also supplies the estimation of the previously mentioned z and x terms, i.e., the topography and the azimuthal position, respectively. Such additional outputs are essential to get the correct location of the targets along the East-West and North-South directions, respectively.

Let us additionally underline that the developed FR SBAS-DInSAR processing chain can be easily adapted, with a few modifications, to inherently deal with SAR data acquired through the TOPS mode, which is used for the IWS acquisition mode of the Sentinel-1 SAR constellation, as schematically depicted in Fig. 3. The peculiar structure into bursts and swaths characterizing the IWS S1 data makes their processing through the FR SBAS pipeline intrinsically parallel with respect to single bursts. Indeed, we can assume each burst as an independent FR P-SBAS processing flow and distribute the overall FR SBAS pipelines corresponding to the native bursts of the considered Sentinel-1 dataset on the different nodes of the exploited computing architecture, discussed in detail in the following Section IV. Clearly, such an intrinsically parallel implementation can be straightforwardly adopted also for the ScanSAR data [63][64], thus making the proposed parallel technique a "general purpose" solution for this kind of "burst" multi-temporal DInSAR dataset.

Finally, we clarify that the presented FR P-SBAS processing chain can be easily applied also when some "linear" phase terms in (7) may not be accurately estimated (Step B of Fig. 2), because of the limited sensitivity of the exploited SAR dataset with respect to the specific parameters. This may occur, for instance, when the Doppler Centroid differences between the SLC images of the interferometric pairs are not significant, or when the phase term associated with the thermal dilation coefficient can be safely assumed negligible, when exploiting SAR sensors with low-frequency bandwidths. In these cases, the thorough model shown in (7) can be then reformed in a simplified version, as follows:

$$\Delta\phi_i^{model} = \frac{4\pi}{\lambda} \frac{b_i^{\perp}}{r \cdot \sin(\theta)} \cdot z + \frac{4\pi}{\lambda} \Delta t_i \cdot v \tag{9}$$

wherein the two "linear" HP phase terms related to the topography z and to the displacement velocity v are accounted for and estimated, only.

IV. The FR P-SBAS Processing Chain

As mentioned before, the FR SBAS algorithm can exploit extensive SAR data archives collected by one or more sensors to retrieve displacement time series of an area of interest. On the other hand, the processing of such large datasets through the conventional FR SBAS processing chain can be computationally inefficient, as it demands a large processing capability. This may pose a severe constraint on effectively exploiting the FR SBAS approach in scenarios where a high

data throughput is required to carry out hazard analyses and implement the associated risk mitigation strategies. Accordingly, to meet the needs of the current EO applications, an efficient implementation of the FR SBAS processing chain, designed to benefit from modern, up-to-date HPC architectures, can find effective exploitation in several application scenarios.

In this framework, we develop an efficient and scalable FR P-SBAS processing chain that, for each processing step, properly exploits the inherent granularity of the processed data and implements an appropriate parallel processing strategy. We jointly apply two different parallelization techniques, referred to as multi-core (CPU-based) and many-core (GPU-based) approaches, respectively. More specifically, in the former, we take advantage of the CPU resources, characterized by a few core architectures, optimized for sequential/serial processing. Indeed, each CPU allows the parallelization of the processing tasks by using a sophisticated methodology based on different synchronization mechanisms among the available CPU cores, to pursue the execution speed-up maximization within sequential programs. Conversely, in the many-core approach we use GPU devices, having a massive, parallel architecture consisting of thousands of less powerful but more efficient cores designed for handling up to thousands of tasks simultaneously [65][66]. In particular, within the developed FR P-SBAS processing chain, we heavily use GPU computation in those steps based on pixel-wise processing (pixel granularity). In contrast, the spatial layer computations (layer granularity) are implemented through multi-core approaches.

In the following, a detailed description of the parallel implementation of all four main steps of the FR-SBAS processing chain is presented, relevant to the Stripmap mode, whose block diagram is shown in Fig. 2. It is worth noting that each processing step is characterized by a specific data granularity that impacts on the selection of the applied architecture-based parallel processing solution, as summarized in Table I.

TABLE I
SAR AND DINSAR DATA GRANULARITY AND EXPLOITED MAIN ARCHITECTURES

Processing Steps	Data Granularity	Main Architecture
A	Layer (Interferogram)	CPU
B	Pixel	GPU
C	Pixel	GPU
D	Layer (SAR acquisition)	CPU

We also remark that the presented parallel implementation can be straightforwardly extended to process the bursts acquired through the TOPS (or ScanSAR) mode, following the lines of the algorithm block diagram shown in Fig. 3.

A. Parallel implementation of the FR SBAS processing chain

Step A of the processing chain shown in Fig. 2 implements two main operations, referred to as: *i)* HP phase component retrieval and *ii)* patch segmentation for stack creation, respectively (see block A in Fig. 2). The first operation consists of the modulo-2π removal of the MR DInSAR phase components from the single-look differential interferograms, aimed to generate the residual HP interferograms. In particular, the inputs of this block are the FR DInSAR interferograms and the MR time series, the latter accounting for both the surface displacement and the atmospheric phase screen components. More specifically, we first compute the MR "synthetic" interferograms by properly recombining the temporal sequences of the time series; subsequently, these interferograms are up-sampled to the full-resolution grid and subtracted from the corresponding single-look interferograms via a modulo-2π operation. All these steps, i.e., the MR synthetic interferogram generation, their up-sampling, the subtraction from the full-resolution interferograms, and the re-wrapping, are carried out on the interferogram (layer) base, representing the operation granularity. Therefore, independent computations, concurrently running on different interferograms, can be easily distributed on multiple processors (CPU multi-cores). Accordingly, dynamic scheduling is performed to distribute the interferogram processing on different cores, where the number of parallel jobs that can be simultaneously launched depends on the available RAM and CPU cores. Note that this procedure can be implemented on both single- and multi-server systems wherein, in this latter case, the independent jobs can benefit from the larger availability of computing cores and memory to maximize the parallelization performance. On the other hand, in this case, the network and storage performance could represent a bottleneck that needs to be properly addressed, particularly when exploiting Cloud Computing environments [34].

The second operation performed in Step A deals with the segmentation of the achieved HP, full-resolution interferograms (layers) into patches, and their subsequent organization into data stacks, which are preparatory inputs of the following two processing steps (i.e., Steps B and C of Fig. 2) implemented through GPU devices. We remark that the patch segmentation procedure is sequential; accordingly, it does not benefit from multi-core systems and mainly relies on the Input/Output performance of the exploited architectures. Note that such a patch segmentation operation is a relevant step aimed at the effective, subsequent exploitation of the GPU devices. In particular, the size of the patches in the azimuth and range directions requires to be set appropriately, by considering the available GPU memory and the peculiarities of the procedure implementation in Step B, as discussed in the following. Once the patch size is defined, the HP residual phase components available on the full-resolution grid are patch-segmented and finally saved as 3D stacks in the disk storage.

Step B in Fig. 2 deals with the estimation of the "linear" HP residual phase components through the maximization of the temporal coherence in (4). This is carried out on a pixel basis, representing the operation granularity, and benefits from a many-core strategy based on GPUs. Such an operation can be easily carried out through nested for-loops, which are relevant to the different linear phase components, see (7). Unfortunately,

such a solution is not particularly effective when using GPU-based architectures. Accordingly, to overcome this issue and to speed-up the processing time, we implement this step as a sequence of matrix operations, which are very effective when implemented via GPUs. Moreover, it is worth to note that the complexity of this processing step also depends upon the number of the exploited model parameters, which can range from two (9) to four (7).

Accordingly, let us first consider the simplified scenario, originally presented in [8] and based on the two-parameter model in (9). In this case, the goal is to search for the optimal pair of topography z_{opt} and velocity v_{opt} from the pre-defined vectors $z = [z_1, z_2, z_3, \dots, z_P]$ and $v = [v_1, v_2, v_3, \dots, v_Q]$, where P and Q identify the search range for the topography z and the velocity v values, respectively. We remark that, for an arbitrary pixel located at (x, r) coordinates, the overall operation in (4) and (9) can be then written, in a matrix formulation, as follows:

$$\max_{v,\Delta z}[T^t \# (V * \Theta)] \tag{10}$$

wherein # and $*$ represent the matrix and the element-wise multiplications, respectively. Furthermore, T, V and Θ are matrices of size M x P, M x Q and M x Q, respectively, defined as follows:

$$T = \begin{bmatrix} e^{-j \cdot ctop_1 \cdot z_1} & \dots & e^{-j \cdot ctop_1 \cdot z_P} \\ \vdots & \ddots & \vdots \\ e^{-j \cdot ctop_M \cdot z_1} & \dots & e^{-j \cdot ctop_M \cdot z_P} \end{bmatrix}$$
$$V = \begin{bmatrix} e^{-j \cdot cvel_1 v_1} & \dots & e^{-j \cdot cvel_1 \cdot v_Q} \\ \vdots & \ddots & \vdots \\ e^{-j \cdot cvel_M \cdot v_1} & \dots & e^{-j \cdot cvel_M \cdot v_Q} \end{bmatrix} \tag{11}$$
$$\Theta = \begin{bmatrix} e^{j \cdot \Delta\phi_1^{HP}} & \dots & e^{j \cdot \Delta\phi_1^{HP}} \\ \vdots & \ddots & \vdots \\ e^{j \cdot \Delta\phi_M^{HP}} & \dots & e^{j \cdot \Delta\phi_M^{HP}} \end{bmatrix}$$

being $ctop_i = \frac{4\pi}{\lambda} \frac{b_i^{\perp}}{r \sin(\theta)}$ and $cvel_i = \frac{4\pi}{\lambda} \Delta t_i$. Note that the above-mentioned procedure is performed on each pixel (x, r), whose processing can be carried out independently from the other pixels.

Some important remarks, regarding the implementation of (10) by using GPUs, are worth to be addressed. We first observe that, though the GPUs are typically equipped with some tens of Gigabytes, their memory is significantly smaller than the RAM of a CPU, which may be equipped with several hundreds of Gigabytes up to Terabytes. Moreover, the data transfer between CPU and GPU, which is needed to execute the operations on GPU devices, is much slower than the RAM access speed and it can significantly jeopardize the GPU performance, if not properly considered. We further underline that, for a given DInSAR dataset, the matrixes Θ and T in (10) and (11) change pixel by pixel and, therefore, they take up the same amount of memory; conversely, the matrix V depends on the temporal baseline Δt_i, whose values do not change with the pixel coordinates and, therefore, the same matrix V is exploited for the whole interferometric analysis. However, under proper hypothesis, we can reasonably consider that also the matrix T does not change from pixel to pixel, thus allowing us to optimize the use of the GPU memory (for instance, in terms of reduced CPU-GPU data transfer [67]). In particular, although $ctop_i$ in (11) changes on a pixel-by-pixel basis, it is a slowly varying parameter and, therefore, we can reasonably assume it as a constant value representative of a spatially limited azimuth/range box. More specifically, in (11), the pixel variations of $b_i^{\perp}$, r and θ can be considered negligible within a reasonable distance. This assumption is very relevant because it allows us to significantly reduce the data transfer between CPU and GPU, which is one of the main overheads in the parallelization of the procedures performed within Step B. By considering the characteristics of the main available SAR systems and the memory usually available in the GPU devices, the 3D DInSAR data stacks can be safely segmented into patches whose sizes typically vary between 1000 and 3000 pixels in both azimuth and range dimensions, whereas we remark that the third dimension of the data stack represents the number of differential interferograms. We further observe that, because the low bandwidth between CPU and GPU negatively impacts the processing performance, we reduce the data transfer between them as much as possible by only moving the input data and the final results. Indeed, for each data patch, all the intermediate results are kept on the GPU memory; therefore, the GPU kernels work without moving any data from/to the CPU until the whole procedure of the analyzed patch is completed, and the results are finally transferred into the CPU memory (RAM).

Furthermore, it is worth noting that the developed algorithm, based on matrix multiplication operations (10) defined for two-dimensional matrixes, is suitable and effective for a 2-parameter estimation; accordingly, it cannot be straightforwardly applied to the more general 4-parameter case (see (6) and (7)). To overcome this issue, within the parallel FR-SBAS interferometric processing chain, Step B is implemented as a cascade of two blocks, where each is devoted to estimating two parameters only. To describe this implementation, let us now assume the model in (7) where, similarly to the simplified case, the aim is to estimate the optimal values, say $[z_{opt}, v_{opt}, x_{opt}, k_{opt}]$, of the 4 linear phase components starting from the pre-defined vectors $z = [z_1, z_2, z_3, \dots, z_P]$, $v = [v_1, v_2, v_3, \dots, v_Q]$, $x = [x_1, x_2, x_3, \dots, x_R]$ and $k = [k_1, k_2, k_3, \dots, k_T]$, where *P*, *Q, R, and T* identify the search range for the topography z, the velocity v, the azimuthal position x and the thermal dilation coefficient k values, respectively. However, because the four HP phase components may not be considered each other independent, due to the possible correlation among the coefficient vectors (as, for instance, in the case of the COSMO-SkyMed constellations, where the temporal and spatial baselines are often coupled due to the orbital maneuvers [68]), different subsets of interferograms for each specific, two-parameter estimation block should be properly selected to maximize the sensitivity of the investigated parameters, and to limit the impact of the

others, as well. An effective way used in the FR P-SBAS processing chain implementation, for such a two blocks cascade operation, is to estimate the topography (z) and the thermal dilation coefficient (k) factors in the first round, and then to proceed with the displacement velocity (v) and the azimuthal position (x) ones in a second one. To do this, the local topography z_{opt} and the thermal dilation k_{opt} optimal terms can be estimated by selecting an appropriate subset of the overall interferograms of the available stacks, characterized by the largest perpendicular baselines of the exploited data pairs (but, in any case, significantly shorter than the critical one), limited temporal baselines (e.g., typically less than 6 months) and nearly zero Doppler Centroid variations. Similarly, once accounted for the phase components related to topography and thermal dilation, the azimuthal position x_{opt} and velocity v_{opt} optimal values can be better estimated by selecting a different subset of the available interferograms characterized by very short perpendicular baselines, to mitigate the spatial decorrelation effects, and by the largest available temporal baseline values, to maximize the displacement sensitivity.

Once estimated and removed the linear terms from the HP residual interferograms, Step C in Fig. 2 addresses the estimation of the residual non-linear HP displacement phase component $d_i^{nl\_res}$, see (8), which can be carried out by solving, through the SVD or Least Square inversion methods, the following linear system of equations:

$$\begin{cases} \langle \Delta\phi_0^{HP}(x,r) - \Delta\phi_0^{model}(x,r)\rangle_{2\pi} = \\ = \dfrac{4\pi}{\lambda}\left[d^{nl_{res}}\left(t_{IE_0},x,r\right) - d^{nl\_res}\left(t_{Is_0},x,r\right)\right] \\ \langle \Delta\phi_1^{HP}(x,r) - \Delta\phi_1^{model}(x,r)\rangle_{2\pi} = \\ = \dfrac{4\pi}{\lambda}\left[d^{nl\_res}\left(t_{IE_1},x,r\right) - d^{nl\_res}\left(t_{Is_1},x,r\right)\right] \\ \vdots \\ \langle \Delta\phi_{M-1}^{HP}(x,r) - \Delta\phi_{M-1}^{model}(x,r)\rangle_{2\pi} = \\ = \dfrac{4\pi}{\lambda}\left[d^{nl\_res}\left(t_{IE_{M-1}},x,r\right) - d^{nl\_res}\left(t_{Is_{M-1}},x,r\right)\right] \end{cases} \quad (12)$$

wherein, as said, (x,r) are the generic azimuth and range coordinates of each pixel, $d^{nl\_res}(\cdot,x,r)$ stands for the LOS-projected residual non-linear HP component of the displacement, $\Delta\phi^{HP} = [\Delta\phi_0^{HP}, \Delta\phi_1^{HP}, \dots, \Delta\phi_{M-1}^{HP}]^T$ and $\Delta\phi^{model} = [\Delta\phi_0^{model}, \Delta\phi_1^{model}, \dots, \Delta\phi_{M-1}^{model}]^T$ are the vectors of the residual HP and the "linear" interferometric phase components corresponding to the M differential interferograms, respectively. Note also that $\mathrm{IS} = [IS_0, IS_1, \dots, IS_{M-1},]^T$ and $\mathrm{IE} = [IE_0, IE_1, \dots, IE_{M-1},]^T$ are the vectors of the acquisition time indexes associated with the primary and secondary images of the interferometric SAR data pairs, respectively. The system in (12) can be also written in a matrix formulation as follows:

$$\Delta\phi^{res} = \left(A \,\#\, d^{\boldsymbol{nl\_res}}\right) \quad (13)$$

being A an incident-like M x N matrix, with M representing the number of interferograms and N the number of SAR acquisitions, where $\forall j = 0, \dots, M-1$, we have $A(j, IS_j) = -1$, $A(j, IE_j) = 1$ and zero otherwise. Moreover, $\Delta\phi^{res} = [\Delta\phi_0^{res}, \Delta\phi_1^{res}, \dots, \Delta\phi_{M-1}^{res}]^T$ is the vector of the differences between the HP and the "linear" interferometric phase components for the M differential interferograms.

Similar to Step B, also Step C is carried out on a pixel basis, representing the operation granularity. Accordingly, also in this case we can extensively exploit GPU architectures. The inputs of this step are the residual HP interferometric stacks $\Delta\phi^{res}$ after the removal of the linear signal phase components relevant to the factors $[\mathrm{z}_{opt}, \mathrm{v}_{opt}, \mathrm{x}_{opt}, \mathrm{k}_{opt}]$, estimated through the previous Step B.

Conventionally, the system is solved by applying the Singular Value Decomposition (SVD) method [6][8]. However, in many real cases, only one interferometric subset is present and the pseudo-inverse formulation [49], in a least square sense, could be straightforwardly applied. In both cases, for each pixel, the HP displacement time series are easily retrieved through GPU-based matrix multiplications. More specifically, in the pseudo-inverse formulation case, we can retrieve the residual non-linear HP displacement components $d^{nl\_res}(\cdot,x,r)$ as follows:

$$d^{nl\_res} = [(A^T \# A)^{-1} \# A^T] \,\#\, \Delta\phi^{res} \quad (14)$$

It is worth noting that the pseudo-inverse matrix $[(A^T \# A)^{-1} \# A^T]$ is common to all pixels of the dataset, therefore the main data transfer toward the GPU device is represented by the residual HP interferometric stacks $\Delta\phi^{res}$.

Finally, Step D in Fig. 2 deals with the computation of the final FR products (displacement time series and the corresponding mean velocity maps). It is worth highlighting that the operations implemented in Step D are independently carried out on a layer basis (i.e., each SAR acquisition epoch), which represents the operation granularity, as for Step A. Therefore, in this procedure the multi-core parallelization strategy implemented through CPUs is applied. More specifically, the considered layer corresponds to the retrieved overall displacement measurements associated to each SAR acquisition epoch. In particular, this Step relies on the MR displacement time series, depurated from the Atmospheric Phase Screen components, which are up sampled to the FR grid and available through the generated segmented patches. Then, the procedure combines the HP linear displacement components, retrieved in Step B, with the non-linear HP displacement term $d^{\boldsymbol{nl\_res}}$, obtained in Step C. Finally, the HP (linear and non-linear) and MR displacement signals are added up, as shown below:

$$\begin{aligned} d(t_n,x,r\,) = {} & d^{LP}(t_n,x,r) + (t_n - t_0)v^{HP}(x,r) \\ & + d^{\boldsymbol{nl\_res}}(t_n,x,r) + k\Delta Temp_n \end{aligned} \quad (15)$$

wherein $n = 0,1,2, \dots, N-1$, with N the number of SAR acquisitions. This allows us to finally retrieve the overall full resolution displacement time series, wherein, we remark,

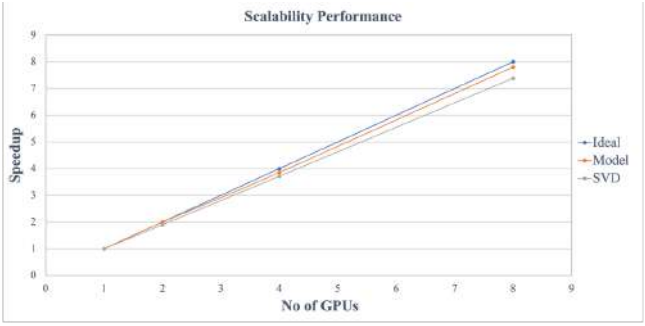

Fig. 4. Speedup curves of the algorithms implemented on GPUs within the FR P-SBAS processing chain. In particular, the blue linear behavior represents the ideal speedup, whereas the orange and the grey curves show the measured speedups relevant to Step B and Step C of the processing chain (see Fig. 2), respectively, as described in Section IV.

$d(t_0, x, r)$ is always assumed equal to zero.

V. Scalability Performance Analysis of the FR P-SBAS Processing Chain

In this paragraph, we present the main outcomes of the analysis carried out to assess the scalability performance of the developed FR P-SBAS processing chain, implemented through the multi-core/many-cores parallelization strategy described in Section IV.A. It is worth noting that a thorough scalability analysis of the MR P-SBAS processing chain, based on a multi-core (CPU-based) parallelization strategy, has already been widely discussed in previous works [33][34]. In particular, by exploiting consolidated metrics, these works have assessed the scalability performance when processing, at medium spatial resolution scale, massive SAR datasets acquired through the Stripmap mode. Therefore, because the multi-core parallel implementation of the FR P-SBAS processing steps strictly follows the same approach, we focus in this Section on the scalability analysis of the FR P-SBAS algorithm implemented through the many-core parallelization strategy, based on the exploitation of multiple GPUs. In this case, we deal with full-resolution SAR datasets, which are split into arbitrarily small patches that are independently processed on multiple GPUs.

The architecture used for the presented scalability analysis consists of four computing nodes of the CNR-IREA processing, each one equipped with 2 CPU AMD EPYC 7513 (32 core, 2.6 GHz) and 2 Nvidia A-100 GPUs with 40 GB of memory, resulting in a total of 8 GPUs. To perform our scalability analysis, we exploited a dataset of overall 1035 differential interferograms generated starting from a sequence of 186 SAR images collected by the sensors of the Italian COSMO-SkyMed first (CSK) and second (CSG) generation constellations from descending orbits (frames HI-01 and STR-003 for CSK and CSG data, respectively) over the Napoli Bay area (Southern Italy), including the Campi Flegrei Caldera volcanic site, chosen as a test site for our experimental analysis. The investigated dataset covers an area of about 32x37 km^2 and has a size of 17000x18000 pixels in the azimuth and range directions, respectively. Taking advantage of the degree of freedom given by the pixel-level granularity of the developed parallel solution, we decided to split the above-mentioned full-resolution interferometric dataset into 306 sub-stacks sized 1000x1000x*Ni* (azimuth, range, number of interferograms), based on the trade-off between the GPU memory occupation and computing time gain. We remark that, as discussed above, the number of interferograms that "feeds" the GPU-based B and C processing Steps of Fig 2 is different according to the proposed parallel implementation. Therefore, within the scalability analysis we accounted for distinct subsets of the overall *Ni* interferograms within Step B and C, without tampering the correctness of the performed procedure.

Before focusing on the GPU-based scalability analysis of Step B and Step C, we first assess the computing time performance of the GPU implementation compared to the CPU-based one. To this aim, we developed a CPU version of the algorithms described in Section IV.A that does not use GPUs, but only CPU resources. We remark that, to implement the CPU version of Step B, we benefit from BLAS and LAPACK libraries [69] to execute the matrix multiplication operations through the CGEMM function. Moreover, as our computing nodes have 64 available cores, we ran the CPU-based software on 60 cores (multi-core strategy) to maximize the achieved performance. The results of such an analysis show that, for what concerns Step B, 60 cores on one server carry out the overall processing in around 661 minutes (i.e., about 11 hours). In contrast, the same operations performed on one GPU are executed in around 162 min (i.e., 2.70 hours), resulting in an almost 4 times improvement of the GPU performance with respect to that of the CPU implementation. Comparable results have been achieved for Step C. These results demonstrate the efficiency improvement achieved by exploiting the many-core parallelization strategy based on GPU devices.

To deeply evaluate the achieved GPU parallel performance, we exploited the Speedup metric [70][71], which quantifies the improvement obtained through the parallel execution with respect to the sequential one. In particular, the speedup S_N relevant to the exploitation of N GPUs is defined as follows [70][71]:

$$S_N = \frac{T_1}{T_N} \tag{16}$$

where T_N *and* T_1 are the execution times relevant to N and 1 GPUs respectively. Obviously, we have $S_N \leq N$, where the equality holds in the ideal case in which there is no source of

TABLE II
Execution Times and Corresponding Measured Speedups for Step B And Step C of the Processing Chain (See Fig. 2) as a Function of the Number of GPUs Exploited in Parallel

No of exploited GPUs	Step B Execution Times [sec]	Step B Speedup	Step C Execution Times [sec]	Step C Speedup
1	9710	**1,00**	3574	**1,00**
2	4870	**1,99**	1881	**1,90**
4	2519	**3,86**	962	**3,71**
8	1245	**7,80**	484	**7,38**

TABLE III
MAIN CHARACTERISTICS OF THE EXPLOITED X-BAND CSK/CSG DATASETS

Acquisition orbit	Ascending	Descending
Wavelenght	3,1 cm	
Acquisition mode	Stripmap	
Spatial resolution [*azimuth x ground range*]	~3 m x 3 m	
Off-nadir angle (*scene center*)	~44°	~24°
Track	HI-16 (CSK) STR-018 (CSG)	HI-01 (CSK) STR-003 (CSG)
Time frame	20 July 2009- 2 December 2023	18 July 2011- 4 December 2023
Number of SAR acquisitions	335	186
Number of overall DInSAR interferograms	1999	1035

efficiency loss or presence of bottlenecks, as well as any overhead due to the parallel computing.

For both Steps B and C of the FR P-SBAS processing chain, we designed the experiments with 1 ,2 ,4 and 8 GPUs to preserve the parallel computation as well balanced as possible within the Speedup analysis. More specifically, in case more than one GPU is used, we conducted the experiments by exploiting 2 GPUs on 1, 2, 3, and 4 nodes, respectively. It is worth noting that the computing HPC infrastructure where we performed the analysis could not be reserved for one user, only, but it is shared with other applications. Therefore, although we select a group of servers that are not involved in intensive processing activity, some bottlenecks related to the use of the network or the shared storage by other jobs could negatively impact and jeopardize the reliability of our results. Accordingly, we carried out several runs for both Steps B and C at different times and averaged the achieved processing times.

To demonstrate the scalability performance of the implemented parallel solution, we show in Fig. 4 the results of our Speedup analysis. In particular, the orange and grey lines represent the achieved Speedups S_N relevant to Step B and Step C, respectively, whereas the blue line corresponds to the ideal Speedup behavior. It is evident that, as the number of GPUs exploited in parallel increases, the deviation of the experimental speedups from the ideal one increases concurrently. More specifically, while the Speedup behavior of Step B is close to the ideal one, the corresponding value for Step C more significantly deviates from it. In general, the discrepancy from the ideal behavior is due to several factors, usually related to the saturation of resources like I/O bandwidth, RAM occupation, and network performance, which can hamper the scalability because these resources are pre-defined and shared among the running jobs. In the case of Step C, as thoroughly discussed in Section IV.A, the I/O operations, as well as the RAM occupation and the data transfer between host and device are more relevant if compared with those involved in Step B. Indeed, the output of Step C consists of some hundreds of 3D sub-stacks (i.e., azimuth, range and time sequences), whereas the results of Step B comprise some 2D matrixes (i.e., azimuth and range dimension). This difference in the size of the outputs becomes more and more relevant as the number of processed images increases, reaching around two orders of magnitude in our specific case study.

Nevertheless, although the size of the processed matrixes could lead to a loss of scalability, the discrepancy between ideal and real behavior in Step C is not so highly impacting the algorithm efficiency, being less than 10% in the worst case (i.e., 8 GPUs). Moreover, by analyzing the values reported in Table II, we can see that the overall processing time needed to complete Step C is, roughly speaking, almost 2.5 times smaller than the corresponding one for Step B. Accordingly, from a broader perspective, the impact of Step C and its bottlenecks are further reduced compared to Step B.

Finally, assuming a real DInSAR scenario where we intend to process a whole CSK/CSG dataset (around 40x40 km^2 for a single frame) consisting of about 200 SAR images, by benefitting from 2 GPUs, the overall time to complete Step B and Step C, which is worth remarking again, are the ones that involve the most computationally intensive operations of the full resolution P-SBAS workflow, is around 112 minutes, i.e., less than 2 hours. Moreover, such computing time can be easily decreased to down 30 minutes by exploiting 8 GPUs.

VI. EXPERIMENTAL RESULTS

This Section is dedicated to presenting the main outcomes of an extensive experimental analysis performed by applying the developed FR P-SBAS processing chain, described in Section IV, over the densely urbanized Napoli Bay (Southern Italy), chosen as area of interest (AOI). In particular, the selected AOI includes the active volcanic site of the Campi Flegrei caldera, which is characterized by an uplift phase restarted in 2005-2006 [72][73]. Due to its valuable natural and anthropogenic heritage, as well as its high level of hazard, related to volcanic and seismic activities occurring in a densely populated zone, this area has been continuously "observed" by several satellite SAR sensors, characterized by different spatial resolutions, frequency bands, acquisition modes and temporal revisit times. This has permitted the collection of thousands of SAR images in the last decades, thus making the Napoli Bay area a unique test zone for remote sensing data exploitation, such as the one proposed in this work. Specifically, we present the results achieved by applying the FR P-SBAS processing chain to some DInSAR datasets acquired over the AOI with different wavelengths (X- and C-band) and acquisition modes (Stripmap and TOPS), aimed to demonstrate the capability of the presented solution to be easily and efficiently adapted to different DInSAR datasets. Moreover, we also show the results of the comparison between the FR P-SBAS displacement time series and the LOS projected ones obtained through the GNSS network of the Italian National Institute of Geophysics and Volcanology (INGV), installed within the Campi Flegrei area [26][74][26].

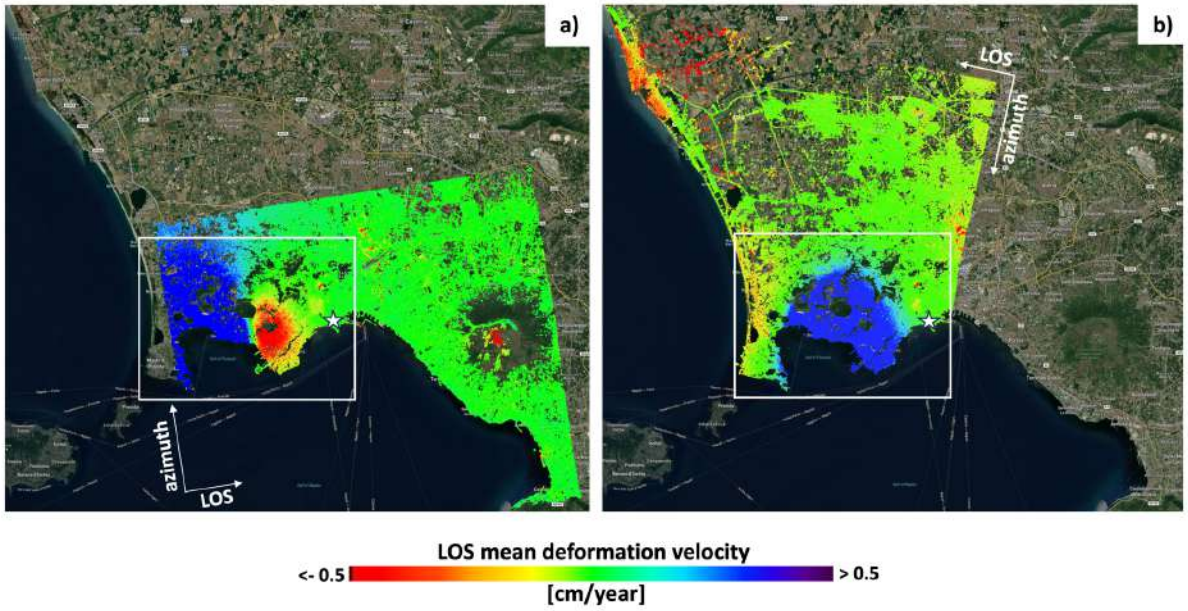

Fig. 5. Full-resolution LOS mean displacement velocity maps, expressed in [cm/year], geocoded and superimposed on an optical image of the Napoli Bay (Italy). The results are relevant to the processing, through the FR P-SBAS pipeline, of the CSK/CSG images relevant to the (a) ascending and (b) descending orbits datasets, whose characteristics are summarized in Table III. The white rectangle identifies the area of the Campi Flegrei caldera, which will be investigated in detail in the following. The white star indicates the position of the reference point, which is located near the Mergellina harbor, within the city of Napoli.

A. CSK/CSG X-band Stripmap data analysis

Let us start this analysis by considering the FR P-SBAS results achieved by processing two X-band, Stripmap SAR datasets collected from ascending and descending orbits over the AOI, by the CSK and CSG sensors, within the MapItaly project of the Italian Space Agency [75]. The ascending dataset is composed of 335 SLC images acquired with a nominal off-nadir angle of 44° (frames HI-16 and STR-018 for CSK and CSG data, respectively) and spanning the July 2009- December 2023 time interval. Moreover, the descending dataset, already used for the scalability analysis presented in Section V, consists of 186 CSK/CSG SAR data acquired between July 2011 and December 2023 with a nominal off-nadir angle of 24° (frames HI-01 and STR-003 for CSK and CSG data, respectively). In Table III we summarize the main characteristics of the two exploited CSK/CSG datasets.

The available SLC images were paired to generate the overall sequences of interferometric SAR data pairs, consisting of a total of 1999 ascending and 1035 descending DInSAR interferograms, respectively. The differential interferograms were selected by imposing a maximum perpendicular baseline of about 1200 m and a maximum temporal baseline of 1800 days. These DInSAR stacks were then split into smaller interferometric subsets to properly feed each single Step within the FR P-SBAS pipeline (see Fig. 2), according to its specific constraint (Section IV.A). We also remark that the 1-arcsec Shuttle Radar Topography Mission (SRTM) DEM was used to remove the large-scale topographic phase component within the DInSAR sequence generation.

The FR P-SBAS processing of such huge interferometric X-band datasets allowed the straightforward generation of the LOS full-resolution displacement time series and of the corresponding mean velocity maps for both the ascending and the descending orbits. In Fig. 5 we present the geocoded mean displacement velocity maps, superimposed on an optical image of the AOI, for the ascending (Fig. 5a) and the descending (Fig. 5b) CSK/CSG datasets, respectively. It is worth noting that the elapsed processing times relevant to the overall parallel FR-SBAS chain carried out by exploiting 4 nodes and a total of 8 GPUs of the CNR-IREA computing facility described in Section V are on the order of 18 and 14 hours for the ascending and descending datasets, respectively.

The displayed maps provide information on the mean velocity values of the LOS displacements associated with the finally resulting coherent pixels, which are more than 16 million and 14 million points for the ascending and descending datasets, respectively. These pixels were identified by imposing a threshold on the temporal coherence factor (4), which provides a quality estimate of the FR P-SBAS displacement time series. In particular, the pixels characterized by a coherence value lower than 0.4 were considered unreliable and then discarded from the results. We also remark that the reference point for both displacement maps is located near the Mergellina harbor, within the city of Napoli, and is identified by a white star in Figs. 5a and 5b.

We underline that the ascending SAR images cover the entire AOI including the urbanized area of the city of Napoli. In contrast, the descending ones are centered on the Campi Flegrei caldera. Accordingly, the ground coverage of the exploited datasets effectively enables the investigation of the large-scale

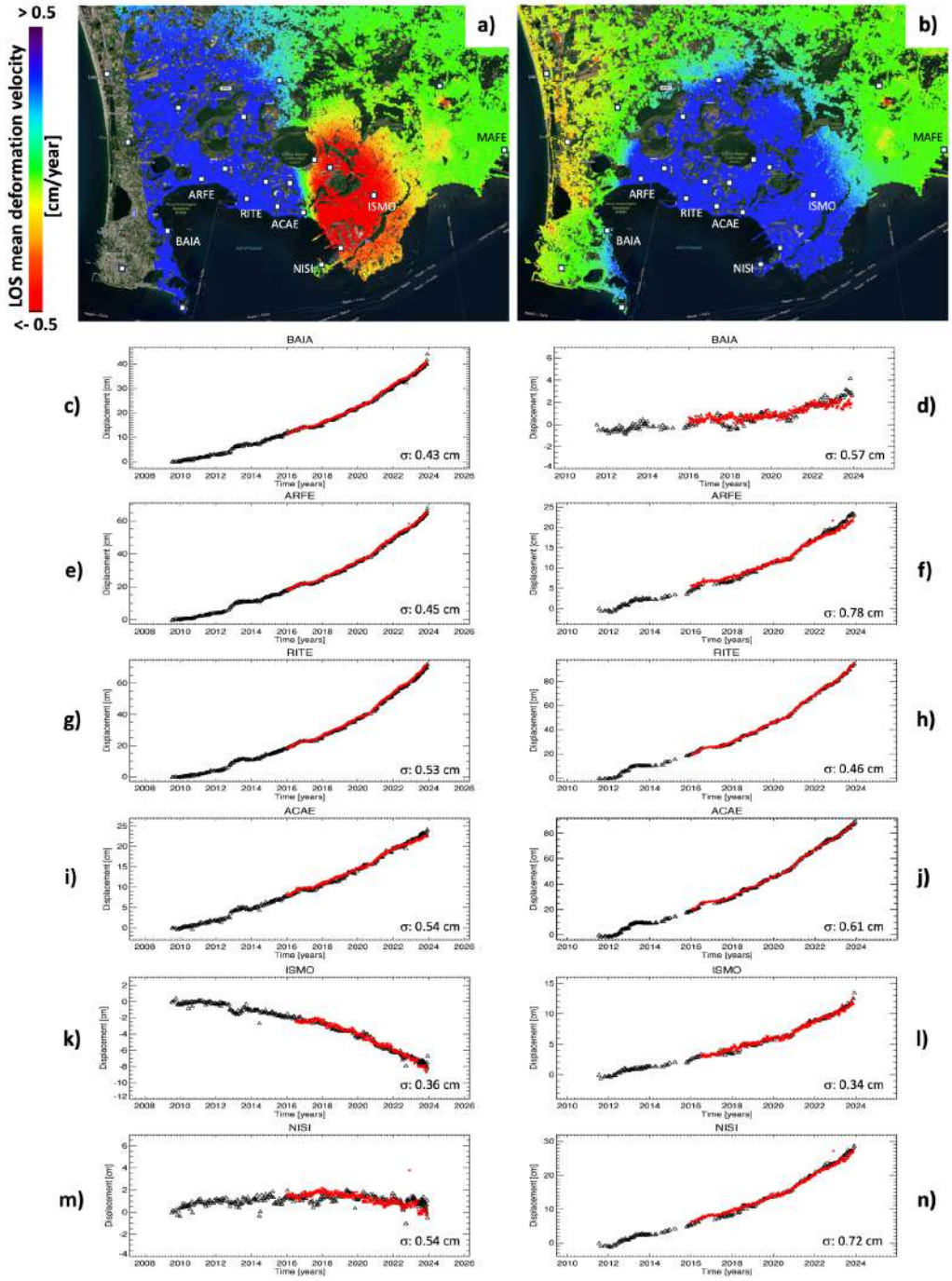

Fig. 6. Comparison between the FR P-SBAS CSK/CSG displacement time series and the LOS-projected ones for a selection of the available GNSS stations of the INGV-OV network [26][74]. (a-b) Zoom-in views of the ascending (a) and descending (b) full-resolution SBAS displacement velocity maps [cm/year], related to the Campi Flegrei caldera (Italy), identified by the white rectangle in Fig. 5 and with superimposed the location of the GNSS stations (white squares). (c-n) Plots of the comparison between the ascending (left column) and descending (right column) DInSAR time series (in black) and the LOS-projected GNSS (in red) measurements in correspondence to 6 selected GNSS stations, labelled as BAIA, ARFE, RITE, ACAE, ISMO and NISI in panels (a-b) and located in the maximum deformation area. Note that the MAFE station (close to the right edge of the investigated area) is set as reference for both FR P-SBAS and GNSS LOS measurements.

displacements affecting the Campi Flegrei caldera (see the white rectangles in Fig. 5), which is the first focus of this experimental analysis. The retrieved deformation patterns are evident, and we highlight them in Fig. 6, which shows the zoom-in views of the mean displacement velocity maps for the ascending (Fig. 6a) and descending (Fig. 6b) orbits, relevant to the caldera edifice. The resulting signals are quite impressive, reaching more than 9 cm/year in the maximum displacement area in correspondence to

TABLE IV
RESULTS OF THE COMPARISON BETWEEN THE FR P-SBAS CSK/CSG AND THE LOS-PROJECTED GNSS DISPLACEMENT TIME SERIES RELEVANT TO THE CAMPI FLEGREI CALDERA [26][74]

GNSS Station	ASC Standard deviation [cm]		DESC Standard deviation [cm]
ACAE	0.54		0.61
AGR1	0.29		N/A
ARFE	0.45		0.78
ASTR	0.38		0.53
BAGN	0.48		0.47
BAIA	0.43		0.57
CMIS	0.50		0.72
CUMA	N/A		0.57
FRUL	0.33		0.43
IPPO	0.54		0.48
ISMO	0.36		0.34
LICO	N/A		0.58
MAFE	0.46		0.46
MORU	0.52		0.58
NISI	0.54		0.72
PIS1	0.34		0.41
QUAR	0.31		0.49
RITE	0.53		0.46
SOLO	0.51		0.74
STRZ	0.37		0.59
VICA	0.45		0.61
Average standard deviation value [cm]	**0.44**		**0.56**

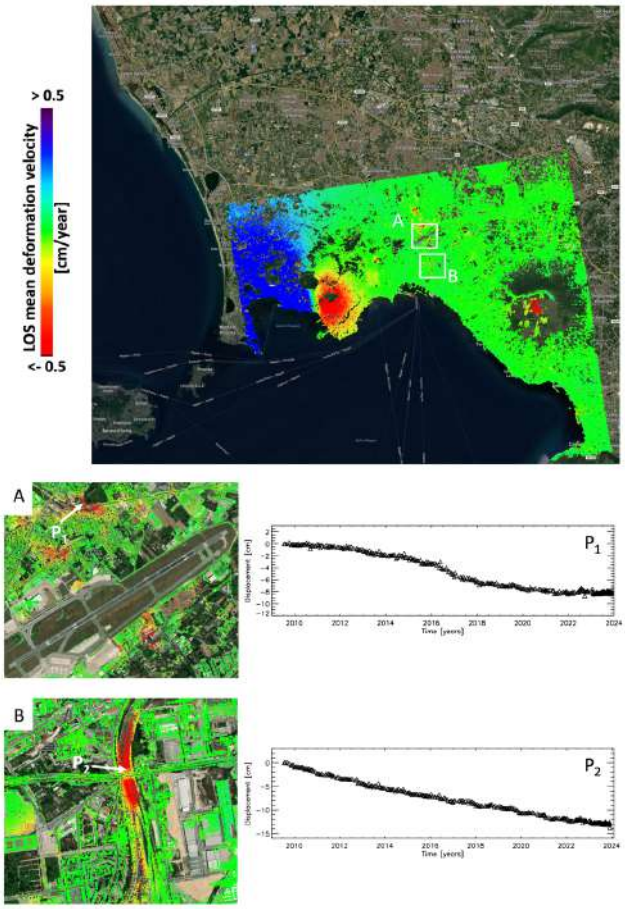

Fig. 7. (Top) Overall FR P-SBAS LOS mean displacement velocity map achieved by processing the ascending CSK/CSG dataset (see Fig. 5a). The white rectangles include two examples related to the Napoli Capodichino airport (A) and the high-speed railway connection (B) areas; the associated FR displacement time series for two pixels, located close to the SP1 highway (P_1), and in correspondence with the high-speed railway link (P_2), characterized by the presence of significant displacements, are also reported.

Rione Terra, nearly in the center of the Pozzuoli Gulf. In Fig. 6, we also indicated the position of the GNSS stations (white squares) of the INGV network within the Campi Flegrei area, which consists of 25 permanent stations [74]. We benefitted from such a network by carrying out an extensive comparative analysis between the FR P-SBAS displacement time series and those retrieved by the LOS-projected measurements of the GNSS stations, aimed to assess the quality of the retrieved DInSAR measurements. Accordingly, we present in Fig. 6 some plots showing the displacement time series retrieved through the developed FR P-SBAS processing chain (black triangles) versus the corresponding LOS-projected GNSS ones (red stars) for the selected stations labelled as BAIA, ARFE, RITE, ACAE, ISMO, and NISI, respectively. We also remark that both the FR P-SBAS and the LOS-projected GNSS displacement time series have been evaluated with respect to a pixel located in correspondence to the MAFE station, close to the Napoli city center, which is sufficiently far from the area of maximum deformation. The obtained results show a very good agreement between the FR P-SBAS and LOS-projected GNSS measurements. For each station of the INGV-OV network located in correspondence to a DInSAR coherent pixel, we have also computed the standard deviation value of the difference between the two deformation time series in the temporal window common to both measurements; the obtained results, relevant to 19 and 20 stations for the ascending and descending datasets (corresponding to coherent DInSAR pixels), respectively, are reported in Table IV, where the average standard deviation values for all the exploited GNSS stations, have been also computed and correspond to 0.44 cm and 0.56 cm for the ascending and descending orbits, respectively.

It is important to point out that, in addition to large-scale displacement analyses, as for the presented one relevant to the Campi Flegrei caldera, in the investigated scenario the implemented FR P-SBAS parallel pipeline is also particularly suitable to be exploited for investigating localized displacement phenomena, such as those affecting single infrastructures and/or buildings. Indeed, for these local-scale analyses the benefits we may capitalize are two-fold: on one side we can exploit the full-resolution DInSAR mapping capabilities of the developed FR P-SBAS approach [76]; on the other one, we can take advantage of the high-resolution characteristics of the exploited X-band SAR data, as well as of the associated precision of the pixel positioning on the planimetric scale, which is on the order of 1–2 m [77], due

TABLE V
MAIN CHARACTERISTICS OF THE EXPLOITED C-BAND SENTINEL-1 DATASET

Acquisition orbit	Ascending
Wavelenght	5.5 cm
Acquisition mode	TOPS
Spatial resolution [*azimuth x ground range*]	~15 m x 5 m
Off-nadir angle (*scene center*)	~35°
Track	44
Time frame	06 May 2016 – 25 January 2024
Number of SAR acquisitions	384
Number of overall DInSAR interferograms	1955

to the significant Doppler Centroid differences among the used SAR data pairs and to the large CSK/CSG orbital tube (almost 2 km). The latter allows us to accurately estimate the residual topographic phase component w.r.t. the Digital Elevation Model (DEM) used in the interferometric processing.

In this framework, several built-up zones affected by localized subsidence patterns have been detected, particularly within the eastward urbanized area of the Napoli town. In the following, we show some examples of the retrieved displacement time series caught thanks to the ascending SAR dataset. More in detail, in Fig. 7 we show two zoom-in views of the FR P-SBAS mean displacement velocity map derived from the processing of CSK/CSG ascending orbits, relevant to the Napoli Capodichino airport (labelled as A) and to the high-speed railway connection (labelled as B) areas in the North-East part of the urban district. Indeed, we can clearly appreciate the high quality of the CSK/CSG results, which show detailed information relevant to most of the buildings and infrastructures located in the investigated zones. This is, for instance, the case of P_1 placed close to the SP1 local highway connection, whose time series, also reported in Fig. 7, shows a rapid acceleration of the LOS displacement trend at the beginning of 2014 followed by a sudden decrease around 2017. Moreover, we can also identify quasi linear displacements as the one related to the pixel P2 located in correspondence to the high-speed railway link close to the Napoli train station, whose LOS time series shows a deformation trend of about 1 cm/year.

These examples represent valuable instances of the FR P-SBAS processing chain capability to identify and analyze the temporal and spatial characteristics of localized displacements related to the built-up environment.

B. Sentinel-1 C-band TOPS data analysis

As already stated in Section III, a peculiarity of the FR P-SBAS algorithm is its inherent capability of working with different SAR acquisition modes besides the classical Stripmap one. This makes

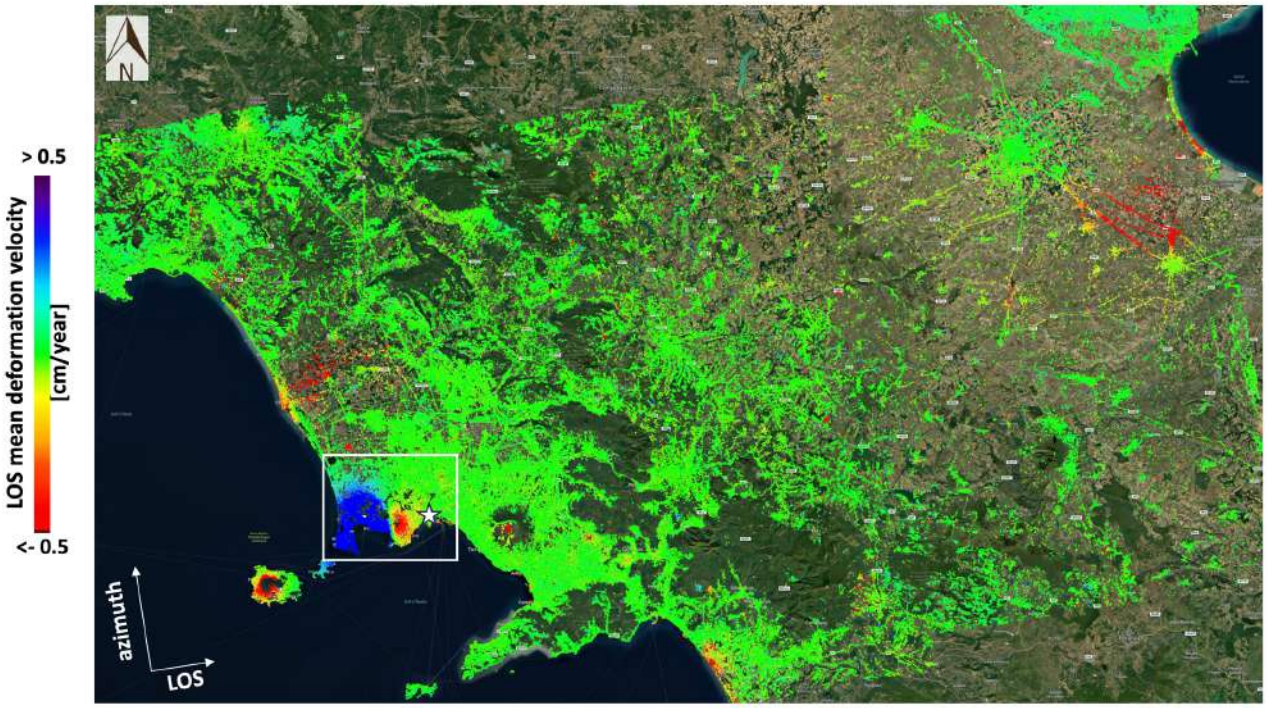

Fig. 8. Full-resolution LOS mean displacement velocity map, expressed in [cm/year], superimposed on an optical image of the investigated area in Southern Italy. The results are relevant to the FR P-SBAS processing of the overall Sentinel-1 frame acquired from ascending orbits (Track 44) in the May 2016-January 2024 time interval. The white rectangle identifies the area of the Campi Flegrei caldera, which will be further investigated (see Fig. 9).

TABLE VI
RESULTS OF THE COMPARISON BETWEEN THE FR P-SBAS SENTINEL-1 AND THE LOS-PROJECTED GNSS DISPLACEMENT TIME SERIES RELEVANT TO THE CAMPI FLEGREI CALDERA [26][74]

GNSS Station	ASC Standard deviation [cm]
ACAE	0.54
AGR1	0.24
ARFE	0.54
ASTR	0.51
BAGN	0.49
BAIA	0.66
CMIS	0.54
CUMA	0.57
FRUL	0.42
IPPO	0.59
ISMO	0.44
LICO	0.49
MAFE	0.47
MORU	0.44
NISI	0.68
PIS1	0.53
QUAR	0.37
RITE	0.61
SOLO	0.49
STRZ	0.55
VICA	0.56
Average standard deviation value [cm]	**0.51**

the presented pipeline a flexible tool to effectively manage and process, with a few simple modifications, the SAR data acquired through the TOPS and ScanSAR modes, which guarantee very large spatial coverage. In this regard, we present in the following the main outcomes deriving from a further experimental analysis conducted by applying the proposed FR P-SBAS processing chain to the archive of C-band Sentinel-1A/1B IWS SAR data acquired in the TOPS mode over a significant portion of Southern Italy, thus encompassing our AOI. Such a DInSAR analysis is aimed at assessing the capability of the implemented parallel solution to efficiently and timely retrieve full-resolution SBAS displacement time series relevant to the overall Sentinel-1 frame that, in the TOPS mode, is characterized by a nominal range footprint extending for about 250 km, thus permitting to easily investigate deformation phenomena at regional and national spatial scales, up to the continental one [27][36][23][78][79].

The exploited Sentinel-1 SAR dataset consists of 384 ascending orbit SLC images, specifically taken from Track 44, collected from May 2016 to January 2024 by the C-band S-1A and S-1B (this latter up to December 2021, when a radar power issue caused the S-1B deorbiting phase) sensors. Note that, in our analysis we avoided to consider the S-1 data between the end of November 2015 and April 2016 because a different version of the IPF was used for the SLC image generation, which can introduce artifacts within the corresponding interferograms due to the incompatibility of this IPF release with respect to subsequent versions [27].

The main characteristics of the analyzed Sentinel-1 dataset are summarized in Table V. We remark that a strategy comparable to the one adopted for the X-band analysis was applied also to generate the overall Sentinel-1 interferometric SAR data pairs and to select the related subsets of interferograms for the linear parameter estimation in Step B. However, as anticipated in Section III, we assert that the azimuthal position cannot be considered in the Sentinel-1 FR P-SBAS processing because of the consistent values of the Doppler Centroids for the S-1 DInSAR data pairs, due to the intrinsic characteristics of the Sentinel-1 constellation. For this reason, we tailored the model in (7) to properly estimate the topography z, the velocity v, and the thermal dilation coefficient κ. Moreover, we imposed a threshold on the maximum temporal baseline (730 days), only, with no constraint on the perpendicular baselines that are intrinsically small in the typical orbital configuration of the Sentinel-1 constellation, with an "orbital tube" of about 200 m [27].

Fig. 8 shows the mosaicked mean displacement velocity map, achieved by processing the full-resolution Sentinel-1 dataset described in Table V through the presented FR P-SBAS approach, superimposed on an optical image of the overall investigated area. Like the previously described X-band analysis, the overall FR P-SBAS chain was carried out by the CNR-IREA computing facility, and the elapsed processing time by exploiting 4 nodes and a total of 8 GPUs is on the order of about 30 hours.

The displayed map covers an area that extends for about 120 x 220 km^2 (about 20 times larger than the exploited CSK/CSG frame) and provides information on the LOS mean displacement velocity values relevant to the finally resulting 15 million coherent pixels. These pixels were selected by considering a temporal coherence threshold of 0.4. Moreover, also in this case the reference point is located near the Mergellina harbor and is highlighted by a white star in Fig. 8.

When comparing Fig. 5a for the CSK/CSG and Fig. 8 for the Sentinel-1 FR P-SBAS analysis, what immediately makes the difference is the impressive ground coverage of the C-band results. This permits the identification of the surface displacement phenomena related to a very extended portion of Southern Italy by processing only one standard Sentinel-1 frame.

On the other hand, we can also observe the similarity, from a qualitative point of view, between the presented Sentinel-1 FR P-SBAS results and those achieved by exploiting the X-band SAR images (Fig. 5a), for what concerns the LOS mean displacement pattern relevant to the common area, due to the comparable off-nadir angles. This is particularly evident when considering again the Campi Flegrei caldera, which is highlighted in the white box of Fig 8 and in its zoom-in view shown in Fig. 9.

To assess the quality of the S-1 FR P-SBAS results, as done for the X-band datasets, we conduct a comparative analysis between the DInSAR displacement time series and the LOS-projected measurements of the GNSS stations of the INGV-OV network [74][26] falling within the AOI (see the velocity map reported in Fig. 9a for their location). The reference pixel for both the FR P-SBAS displacement time series and the LOS-projected GNSS measurements is again set to the MAFE station, close to the Napoli city center, which, as said, is sufficiently far from the maximum deformation area.

For 10 selected stations located within the Campi Flegrei caldera and labelled as BAIA, ARFE, STRZ, RITE, PIS1, ACAE,

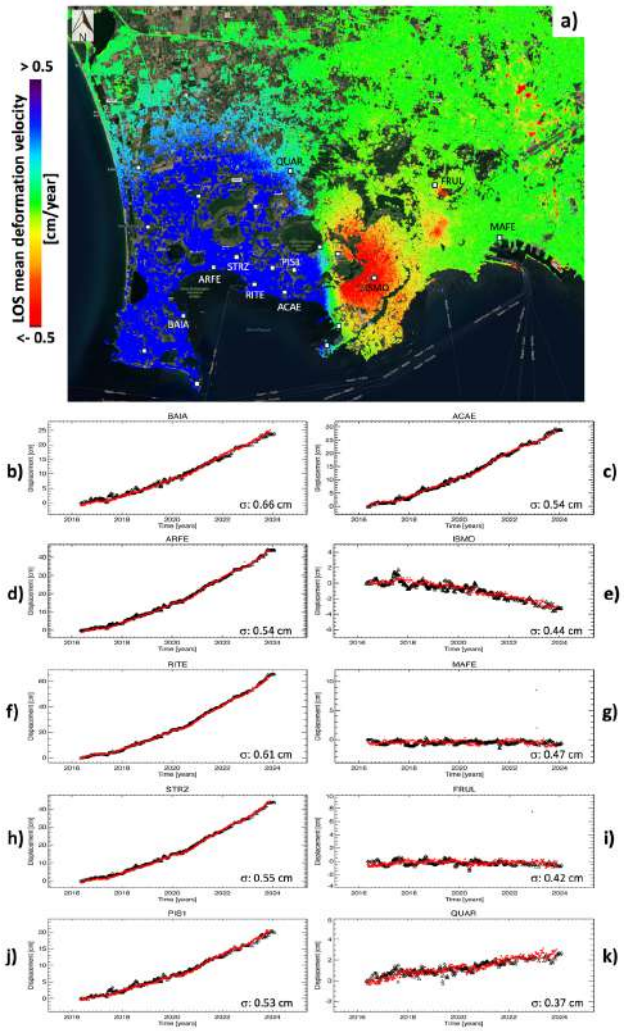

Fig. 9. Comparison between the FR P-SBAS Sentinel-1 displacement time series and the LOS-projected ones for a selection of the available GNSS stations of the INGV-OV network [26][74]. (a) Zoom-in view of the ascending full-resolution SBAS displacement velocity map [cm/year], related to the Campi Flegrei caldera (Italy), identified by the white rectangle in Fig. 8 and with superimposed the location of the GNSS stations (white squares). (b-j) Plots of the comparison between the DInSAR time series (black triangles) and the LOS-projected GNSS measurements (red stars) in correspondence to 10 selected GNSS stations, labelled as BAIA, ARFE, STRZ, RITE, PIS1, ACAE, ISMO, MAFE, FRUL and QUAR and located in the maximum displacement area. Note that the MAFE station is set as a reference for both FR P-SBAS and GNSS LOS measurements.

ISMO, MAFE, FRUL, and QUAR, we report in Figs 9-(b-k) the graphs of the comparison between the FR P-SBAS displacement time series (black triangles) and the corresponding LOS-projected GNSS measurements (red stars). The very good agreement between the two displacement time series is quite evident, as also confirmed by the standard deviation values of their difference in the temporal window common to both measurements, computed for 21 GNSS stations of the INGV-OV network located in correspondence to the DInSAR coherent pixels. Moreover, the average standard deviation value computed for all the exploited 21 GNSS stations corresponds to 0.51 cm (see Table VI).

Finally, we investigate, through a qualitative analysis between the CSK/CSG and the S-1 FR P-SBAS results, the capability of the exploited X- and C-band SAR datasets to correctly geolocate the identified coherent pixels. In particular, by comparing the X- and C-band FR P-SBAS velocity maps, shown in the zoom-in views of Fig. 10a and 10b, respectively, and relevant to the SS87 highway located in the Northern part of the city of Napoli, it is quite evident that the Sentinel-1 measurements largely suffer from a rather limited accuracy in the correct pixel positioning in a cartographic/geographic reference system, with respect to the corresponding CSK/CSG products. This is mainly due to the absence of significant Doppler Centroid differences among the used SAR data pairs and to the small "orbital tube" of the Sentinel-1 constellation. The former limits the geolocation accuracy mostly in the North-South direction, while the latter leads to a drastic reduction of the maximum perpendicular baseline among all the possible interferometric pairs compared to other SAR systems intrinsically devoted to high-resolution applications (as in the case of CSK/CSG SAR constellation); this results in a significant accuracy loss in estimating the residual topographic phase

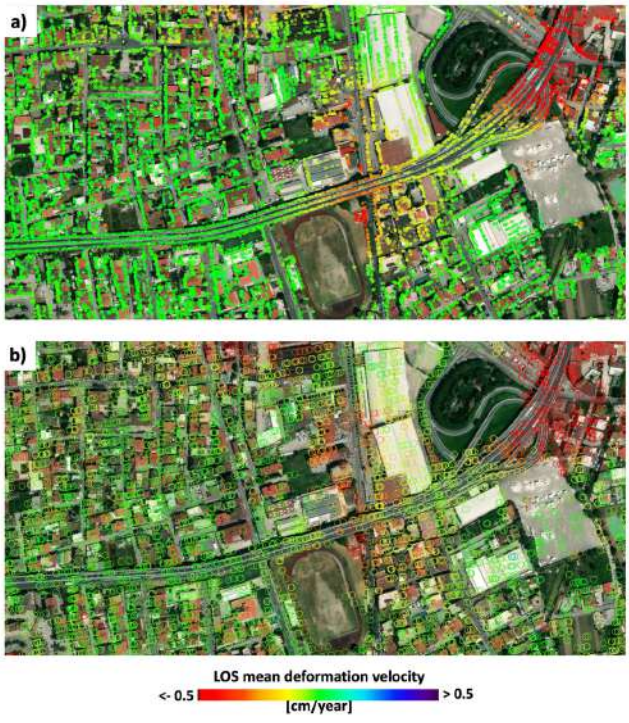

Fig. 10. Comparative analysis between the CSK/CSG (a) and the S-1 (b) FR P-SBAS results relevant to the SS87 highway located in the Northern part of the city of Napoli, in terms of capability to correctly geolocate the identified coherent pixels. Note that, to account for the different (full) spatial resolutions of the CSK/CSG and S-1 sensors, we represent the corresponding pixels by means of circles with a radius of 3 m and 10 m, respectively.

component z with respect to the Digital Elevation Model (DEM) used in the interferometric processing, thus leading to a less accurate pixel planar positioning, mostly in the East-West direction. However, we underline that the recent thruster anomaly of the Sentinel-1A system [80] is leading to an unavoidable increase of the baseline tube for these data that can be exploited, in the near future, to improve the geolocation accuracy of the generated full-resolution DInSAR products, thus turning a system limitation into a potential future opportunity for some Sentinel-1 DInSAR applications.

VII. Conclusion and Further Developments

We presented an advanced parallel implementation of the full-resolution SBAS processing chain for the automatic and efficient retrieval of displacement time series, which allows us to effectively investigate the phenomena affecting wide areas, as well as single buildings and infrastructures. We started with some algorithmic advancements, primarily aimed at improving the quality of the full-resolution DInSAR time series. Furthermore, we focused on a parallel implementation of the processing chain, carried out through the efficient exploitation of innovative parallel technologies, with a key effort devoted to the use of the GPU devices. The presented analysis demonstrates that such devices are very effective in significantly reducing the processing time needed to the FR P-SBAS processing chain to compute full-resolution displacement time series from large DInSAR datasets. In particular, we proved that the implemented solution has excellent Speedup performance and high scalability. More specifically, by exploiting up to 8 GPUs, we completed the FR P-SBAS processing of a CSK/CSG full-frame (with more than 300 SAR acquisitions) in less than 18 hours. We remark that the benefits of using GPU-based architectures to significantly reduce computing times are already known in several applications. However, due to the high cost of these devices, their availability in general purposes computing facilities was not widespread. Nowadays, thanks to the latest advances in Artificial Intelligence applications, based on the large exploitation of GPU computations, the cost of these devices is rather rapidly decreasing, with a parallel increase in performance, making them easily accessible even in relatively small HPC infrastructures and Cloud Computing environments designed for a wide range of applications. We also remark that, even if technical issues related to power consumption and heat dispersion make the installation of several GPU devices on the same server not commonplace, the up-to-date technology in this sector is moving towards, setting up servers equipped with 8 or more GPU devices. Accordingly, such a scenario makes the proposed FR P-SBAS solution quite timely, flexible and easy to implement in a wide range of HPC infrastructures and Cloud Computing platforms.

It is also worth noting that although the developed parallel implementation of the FR SBAS processing chain has been originally tailored to the SAR data collected with the Stripmap acquisition mode, it can also be straightforwardly applied to process large DInSAR data stacks collected with different acquisition modes, such as the ScanSAR and TOPS ones. Concerning this point, we have shown that the efficiency achieved with Stripmap CSK/CSG datasets is basically preserved also when dealing with Sentinel-1 DInSAR data relevant to the TOPS acquisition mode. Indeed, by exploiting up to 8 GPU devices, we completed the FR P-SBAS processing of a Sentinel-1 full-frame (with nearly 400 images) in about 30 hours.

In order to assess the quality of the DInSAR products generated through the proposed FR P-SBAS solution, an extensive experimental analysis was also carried out. This is based on exploiting long sequences of X-band COSMO-SkyMed Stripmap and C-band Sentinel-1 TOPS acquisitions, mostly relevant to the Campi Flegrei Caldera volcanic site, which is located within the Napoli Bay area (Southern Italy) and is monitored through a dense GNSS network. Through a comparative analysis with GNSS measurements, the presented results demonstrate the effectiveness of the implemented FR P-SBAS processing in retrieving, from the exploited multi-frequency and multi-platform SAR data, displacement time series with sub-centimetric accuracy generated at their full spatial resolution. Moreover, we also underline the very detailed spatial information and precise geolocation peculiarities of the CSK/CSG DInSAR products, thanks to the high spatial resolutions, as well as to the large perpendicular baseline tube and the Doppler Centroid variations characterizing the different sensors of this X-band SAR constellation.

Future developments of our work concern the portability of the proposed solution in Cloud Computing environments. Indeed, the current scenario is rapidly evolving towards a strong integration of advanced DInSAR applications within Cloud Computing e-infrastructures. With this respect, we underline that the parallel implementation proposed in this work can be easily adapted and optimized to benefit from Cloud Computing environments. However, the impact of some bottlenecks deriving from the exploitation of these platforms, such as the network constraints and the storage performance, needs to be deeply investigated to address the massive and systematic Cloud Computing application of the proposed parallel solution. We further remark that the implemented FR P-SBAS solution is suitable to be made available to the users through initiatives like GEP [81] and Earth Console [82] that, until now, have been limited to the generation of MR DInSAR products through the SBAS approach.

We finally stress that the developed FR P-SBAS processing chain may play a key role in exploiting DInSAR data acquired by the recently operating and the upcoming SAR systems and constellations. This is, for instance, the case of the new L-band SAR sensors such as the SAOCOM-1 constellation [83][84] and the ALOS-4 systems [85], as well as for the forthcoming (NASA-ISRO) NISAR mission [86]. Moreover, a major impact is also foreseen for what concerns the DInSAR exploitation of the new small satellite constellations, as for the case of the Italian 12 X-band small satellite NIMBUS-IRIDE Medium Inclination Orbit constellation [87], which is expected to be fully deployed in orbit between 2025 and 2026.

Acknowledgment

The Digital Elevation Model of the analyzed areas was acquired through the NASA SRTM archive. This article contains modified Copernicus Sentinel data 2024. The

European Commission, Copernicus Programme, and ESA's contribution to the systematic Sentinel-1 data acquisitions and open data policy are greatly appreciated. The authors acknowledge the Italian Space Agency (ASI) for acquiring and providing the COSMO-SkyMed (CSK and CSG) data under the ASI-IREA License to Use Agreement (ID 809 ASI Project Card). The GNSS measurements have been provided by the Italian National Institute of Geophysics and Volcanology (INGV).

REFERENCES

[1] K. Gabriel, R. M. Goldstein, and H. A. Zebker, "Mapping small elevation changes over large areas: differential radar interferometry," J Geophys Res, 1989, doi: 10.1029/JB094iB07p09183.

[2] P. A. Rosen, Hensley, S., Joughin, I. R., Li, F. K., Madsen, S. N., Rodriguez, E. and Goldstein R. M., "Synthetic aperture radar interferometry," Proceedings of the IEEE, vol. 88, no. 3, 2000, doi: 10.1109/5.838084.

[3] D. Massonnet, and Feigl, K.L., "Radar interferometry and its application to changes in the Earth's surface," Rev. Geophys., 36, 441–500, 1998.

[4] R. Burgmann, P. A. Rosen, and E. J. Fielding, "Synthetic aperture radar interferometry to measure earth's surface topography and its deformation," Annu Rev Earth Planet Sci, vol. 28, 2000, doi: 10.1146/annurev.earth.28.1.169.

[5] A. Ferretti, C. Prati, and F. Rocca, "Nonlinear subsidence rate estimation using permanent scatterers in differential SAR interferometry," *IEEE Trans. Geosci. Remote Sens.*, vol. 38, no. 5 I, 2000, doi: 10.1109/36.868878.

[6] P. Berardino, G. Fornaro, R. Lanari, and E. Sansosti, "A new Algorithm for Surface Deformation Monitoring based on Small Baseline Differential SAR Interferograms", *IEEE Trans. Geosci. Remote Sens.* 40, 11, 2375-2383, 2002.

[7] C. Werner, U. Wegmüller, T. Strozzi, and A. Wiesmann, "Interferometric Point Target Analysis for Deformation Mapping," in International Geoscience and Remote Sensing Symposium (IGARSS), 2003. doi: 10.1109/igarss.2003.1295516.

[8] R. Lanari, O. Mora, M. Manunta, J. J. Mallorquì, P. Berardino, and E. Sansosti, "A small-baseline approach for investigating deformations on full-resolution differential SAR interferograms", *IEEE Trans. Geosci. Remote Sens.,* 42, 7, 1377–1386, 2004.

[9] M. Crosetto, B. Crippa, and E. Biescas, "Early detection and in-depth analysis of deformation phenomena by radar interferometry", *Engineering Geology,* 79, 81–91, 2005 doi: 10.1016/j.enggeo.2004.10.016.

[10] A. J. Hooper, "A multi-temporal InSAR method incorporating both persistent scatterer and small baseline approaches," Geophys Res Lett, vol. 35, no. 16, 2008, doi: 10.1029/2008GL034654.

[11] A. Ferretti, A. Fumagalli, F. Novali, C. Prati, F. Rocca, and A. Rucci "A New Algorithm for Processing Interferometric Data- Stacks: SqueeSAR". *IEEE Trans. Geosci. Remote Sens*., 49, 3460 – 3470, 2011

[12] H. A. Zebker and J. Villasenor, "Decorrelation in interferometric radar echoes," *IEEE Trans. Geosci. Remote Sens.*, vol. 30, no. 5, 1992, doi: 10.1109/36.175330.

[13] R. Lanari, et al., "Evidence for a peculiar style of ground deformation inferred at Vesuvius volcano," Geophys. Res. Lett., vol. 29, no. 9, pp. 6-1–6-4, 2002. doi: 10.1029/2001GL014571.

[14] R. Lanari, Casu, F., Manzo, M., and Lundgren, P., "Application of the SBAS-DInSAR technique to fault creep: A case study of the Hayward fault, California," Remote Sensing of Environment, 109(1), 20-28, 2007

[15] R. Lanari et al., "Surface displacements associated with the L'Aquila 2009 Mw 6.3 earthquake (central Italy): New evidence from SBAS-DInSAR time series analysis," Geophys Res Lett, vol. 37, no. 20, 2010, doi: 10.1029/2010GL044780.

[16] A. Manconi et al., "On the effects of 3-D mechanical heterogeneities at Campi Flegrei caldera, southern Italy," J. Geophys. Res., Space Phys., vol. 115, no. 8, 2010, Art. no. B08405. doi: 10.1029/2009JB007099.

[17] F. Calò et al., "Enhanced landslide investigations through advanced DInSAR techniques: The Ivancich case study, Assisi, Italy", Remote Sens. Environ., vol. 142, pp. 69–82, Feb. 2014, doi: 10.1016/j.rse.2013.11.003.

[18] E. Sansosti et al., "How second generation SAR systems are impacting the analysis of ground deformation," International Journal of Applied Earth Observation and Geoinformation, vol. 28, no. 1, 2014, doi: 10.1016/j.jag.2013.10.007.

[19] Q. Zhao et al., "A DInSAR investigation of the ground settlement time evolution of ocean-reclaimed lands in Shanghai", IEEE J. Sel. Topics Appl. Earth Observ. Remote Sens., vol. 8, no. 4, pp. 1763– 1781, Apr. 2015, doi: 10.1109/JSTARS.2015.240216.

[20] F. Diao et al., "Fault locking near Istanbul: indication of earth- quake potential from InSAR and GPS observations," Geophys. J. Int., vol. 205, pp. 490–498, Feb. 2016, doi: 10.1093/gji/ggw048.

[21] S. Scifoni et al., "On the joint exploitation of long-term DInSAR time series and geological information for the investigation of ground settlements in the town of Roma (Italy)", Remote Sens. Environ., vol. 182, pp. 113–127, Sep. 2016, doi: 10.1016/j.rse.2016.04.017.

[22] G. Calamita, et al., "An integrated geophysical approach for urban underground characterization: the Avigliano town (southern Italy) case study," Geomatics, Natural Hazards and Risk, 10(1), 412-432, 2009

[23] R. Lanari, et al., "Automatic generation of Sentinel-1 continental scale DInSAR deformation time series through an extended P-SBAS processing pipeline in a cloud computing environment," Remote Sensing, vol. 12, no. 18, 2020, doi: 10.3390/RS12182961.

[24] F. Cigna, R. E. Ramírez, and D. Tapete, "Accuracy of sentinel-1 PSI and SBAS InSAR displacement velocities against GNSS and geodetic leveling monitoring data," Remote Sensing, vol. 13, no. 23, 2021, doi: 10.3390/rs13234800.

[25] F Di Traglia, C De Luca, M Manzo, T Nolesini, N Casagli, R Lanari, F Casu, "Joint exploitation of space-borne and ground-based multitemporal InSAR measurements for volcano monitoring: The Stromboli volcano case study", Remote Sensing of Environment 260, 112441, 2021, https://doi.org/10.1016/j.rse.2021.112441.

[26] F. Giudicepietro, F. Casu, M. Bonano, C. De Luca, P. De Martino, F. Di Traglia, M.A. Di Vito, G. Macedonio, M. Manunta, F. Monterroso, P. Striano and R. Lanari "First Evidence of a Geodetic Anomaly in the Campi Flegrei Caldera (Italy) Ground Deformation Pattern Revealed by DInSAR and GNSS Measurements During the 2021-2023 Escalating Unrest Phase, " *International Journal of Applied Earth Observation and Geoinformation*, Vol. 132, 104060, 2024, https://doi.org/10.1016/j.jag.2024.104060

[27] M. Manunta et al., "The Parallel SBAS Approach for Sentinel-1 Interferometric Wide Swath Deformation Time-Series Generation: Algorithm Description and Products Quality Assessment," *IEEE Trans. Geosci. Remote Sens.*, vol. 57, no. 9, pp. 6229–6281, 2019, doi: 10.1109/TGRS.2019.2904912.

[28] A. Pepe, Y. Yang, M. Manzo, and R. Lanari, "Improved EMCF-SBAS processing chain based on advanced techniques for the noise-filtering and selection of small baseline multi-look DInSAR interferograms", *IEEE Trans. Geosci. Remote Sens.*, vol. 53, no. 8, 2015, doi: 10.1109/TGRS.2015.2396875.

[29] C. De Luca, F. Casu, M. Manunta, G. Onorato and R. Lanari, "Comments on "Study of Systematic Bias in Measuring Surface Deformation With SAR Interferometry"," *IEEE Trans. Geosci. Remote Sens.*, vol. 60, pp. 1-5, 2022, doi: 10.1109/TGRS.2021.3103037.

[30] H. Ansari, F. De Zan, and A. Parizzi, "Study of Systematic Bias in Measuring Surface Deformation With SAR Interferometry," *IEEE Trans. Geosci. Remote Sens.*, vol. 59, no. 2, pp. 1285–1301, Feb. 2021, doi: 10.1109/TGRS.2020.3003421.

[31] M. Manunta, Marsella, M., Zeni, G., Sciotti, M., Atzori, S., and Lanari, R., "Two-scale surface deformation analysis using the SBAS-DInSAR

technique: a case study of the city of Rome, Italy," International Journal of Remote Sensing, 29(6), 1665-1684, 2008.

[32] M. Bonano, M. Manunta, M. Marsella, and R. Lanari, "Long-term ERS/ENVISAT deformation time-series generation at full spatial resolution via the extended SBAS technique," Int J Remote Sens, 2012, doi: 10.1080/01431161.2011.638340.

[33] F. Casu et al., "SBAS-DInSAR parallel processing for deformation time-series computation," IEEE J. Sel. Top. Appl. Earth Obs. Remote Sens., vol. 7, no. 8, 2014, doi: 10.1109/JSTARS.2014.2322671.

[34] I. Zinno; Casu, F.; De Luca, C.; Elefante, S.; Lanari, R.; Manunta, M., "A Cloud Computing Solution for the Efficient Implementation of the P-SBAS DInSAR Approach," *IEEE J. Sel. Top. Appl. Earth Obs. Remote Sens.*, 2017, 10, 802–817.

[35] I. Zinno; Elefante, S.; Mossucca, L.; De Luca, C.; Manunta, M.; Terzo, O.; Lanari, R.; Casu, F., "A First Assessment of the P-SBAS DInSAR Algorithm Performances Within a Cloud Computing Environment," *IEEE J. Sel. Top. Appl. Earth Obs. Remote Sens.*, 8, 4675–4686, 2015

[36] I Zinno, M Bonano, S Buonanno, F Casu, C De Luca, M Manunta, M Manzo, R Lanari, "National scale surface deformation time series generation through advanced DInSAR processing of sentinel-1 data within a cloud computing environment", IEEE Transactions on Big Data 6 (3), 558-571, 2018, doi: 10.1109/TBDATA.2018.2863558

[37] Wu, Z.; Lv, X.; Yun, Y.; Duan, W. A Parallel Sequential SBAS Processing Framework Based on Hadoop Distributed Computing," Remote Sensing, 16, 466, 2024. https://doi.org/10.3390/rs16030466

[38] A. Guerriero, V. W. Anelli, A. Pagliara, R. Nutricato and D. O. Nitti, "Efficient implementation of InSAR time-consuming algorithm kernels on GPU environment," 2015 IEEE International Geoscience and Remote Sensing Symposium (IGARSS), Milan, Italy, 2015, pp. 4264-4267, doi: 10.1109/IGARSS.2015.7326768.

[39] N. Shamsaldin et al, "The Influence of SIMD Architecture on the Efficiency of Parallel Processing Approaches: From Web and AI Perspective", JITI, vol. 3, no. 1, Apr. 2024.

[40] C. De Luca, I. Zinno, M. Manunta, R. Lanari, and F. Casu, "Large areas surface deformation analysis through a cloud computing P-SBAS approach for massive processing of DInSAR time series," Remote Sensing of Environment, vol. 202, pp. 3–17, 2017, doi: 10.1016/j.rse.2017.05.022.

[41] M. Di Bisceglie, Di Santo, M., Galdi, C., Lanari, R., & Ranaldo, N., "Synthetic aperture radar processing with GPGPU," IEEE Signal Processing Magazine, 27(2), 69-78, 2010.

[42] A. Rogan and R. Carande, "InSAR processing using a GPGPU," Proc. SPIE 8051, Algorithms for Synthetic Aperture Radar Imagery XVIII, 4 May 2011, https://doi.org/10.1117/12.889917

[43] D. Romano, and M. Lapegna. "A GPU-parallel image coregistration algorithm for InSar processing at the edge," Sensors, 21, 17, 5916, 2021.

[44] F. De Zan and A. M. Guarnieri, "TOPSAR: Terrain observation by progressive scans," *IEEE Transactions on Geoscience and Remote Sensing*, vol. 44, no. 9, 2006, doi: 10.1109/TGRS.2006.873853.

[45] R. Torres et al., "GMES Sentinel-1 mission," Remote Sens Environ, vol. 120, 2012, doi: 10.1016/j.rse.2011.05.028.

[46] M. Bonano et al., "Advanced Implementation of the Full Resolution P-SBAS DInSAR Processing Chain Based on Scalable GPU-Parallel Techniques for the Efficient Deformations Analysis of the Built-Up Environment," in 2022 IEEE International Geoscience and Remote Sensing Symposium, Kuala Lumpur, Malaysia, pp. 1103-1106, 2022, doi: 10.1109/IGARSS46834.2022.9884443.

[47] M. Bonano et al., "First and Second Generation Cosmo-Skymed Advanced DInSAR Processing for Investigating Deformations Affecting The Built-up Environment," in 2023 IEEE International Geoscience and Remote Sensing Symposium, Pasadena, CA, USA, pp. 1842-1845, 2023, doi: 10.1109/IGARSS52108.2023.10283194.

[48] A. Pepe and R. Lanari, "On the extension of the minimum cost flow algorithm for phase unwrapping of multitemporal differential SAR interferograms," *IEEE Trans. Geosci. Remote Sens.*, vol. 44, no. 9, pp. 2374–2383, 2006, doi: 10.1109/TGRS.2006.873207

[49] G. Strang, Linear Algebra and Its Applications. Orlando, FL: Harcourt Brace Jovanovich, 1988

[50] A. Pepe, Berardino, P., Bonano, M., Euillades, L. D., Lanari, R., and Sansosti, E., "SBAS-based satellite orbit correction for the generation of DInSAR time-series: Application to RADARSAT-1 data," *IEEE Trans. Geosci. Remote Sens.*, 49(12), 5150-5165, 2011

[51] B. M. Kampes, "Radar interferometry - Persistent Scatterer Technique," Vol. 12. Dordrecht, The Netherlands: Springer, 2006. doi: 10.1007/978-1-4020-4723-7.

[52] M. Crosetto, O. Monserrat, M. Cuevas-González, N. Devanthéry, and B. Crippa, "Persistent Scatterer Interferometry: A review," ISPRS Journal of Photogrammetry and Remote Sensing, 115, 78-89, 2016. doi: 10.1016/j.isprsjprs.2015.10.011.

[53] N. Miranda, Rosich, B., Santella, C. and Grion, M., "Review of the impact of ERS-2 piloting modes on the SAR Doppler stability," in Proceedings Fringe '03, 1–5 December 2003, Frascati, Italy [online]. Available:https://earth.esa.int/eogateway/documents/20142/37627/Review-impact-ERS-2-Piloting-Modes-SAR-Doppler-Stability26-miranda.pdf

[54] M. Bonano, Manunta, M., Pepe, A., Paglia, L., and Lanari, R., "From previous C-band to new X-band SAR systems: Assessment of the DInSAR mapping improvement for deformation time-series retrieval in urban areas," *IEEE Trans. Geosci. Remote Sens.*, 51(4), 1973-1984, 2013.

[55] M. Crosetto, O. Monserrat, and G. Herrera, "Urban applications of persistent scatterer interferometry," Remote Sensing and Digital Image Processing, vol. 15, 2010. doi: 10.1007/978-90-481-3751-0_10.

[56] M. Crosetto, O. Monserrat, M. Cuevas-González, N. Devanthéry, G. Luzi, and B. Crippa, "Measuring thermal expansion using X-band persistent scatterer interferometry," ISPRS Journal of Photogrammetry and Remote Sensing, vol. 100, 2015, doi: 10.1016/j.isprsjprs.2014.05.006.

[57] O. Monserrat, M. Crosetto, M. Cuevas, and B. Crippa, "The thermal expansion component of persistent scatterer interferometry observations," IEEE Geoscience and Remote Sensing Letters, vol. 8, no. 5, pp. 864-868, Sept. 2011, doi: 10.1109/LGRS.2011.2119463.

[58] G. Fornaro, D. Reale, and S. Verde, "Monitoring thermal dilations with millimetre sensitivity via multi-dimensional SAR imaging," in Proceedings of the 2012 Tyrrhenian Workshop on Advances in Radar and Remote Sensing: From Earth Observation to Homeland Security, TyWRRS 2012, 2012. doi: 10.1109/TyWRRS.2012.6381117.

[59] J. Zhu and Q. Meng, "Effective and Fine Analysis for Temperature Effect of Bridges in Natural Environments," Journal of Bridge Engineering, vol. 22, no. 6, 2017, doi: 10.1061/(asce)be.1943-5592.0001039.

[60] X. Qin, L. Zhang, M. Yang, H. Luo, M. Liao, and X. Ding, "Mapping surface deformation and thermal dilation of arch bridges by structure-driven multi-temporal DInSAR analysis," Remote Sens Environ, vol. 216, 2018, doi: 10.1016/j.rse.2018.06.032.

[61] X. Zhu and R. Bamler, "Let's do the time warp: Multicomponent non-linear motion estimation in differential SAR tomography," IEEE Geosci. Remote Sens. Lett., vol. 8, no. 4, pp. 735–739, Jul. 2011.

[62] D. Reale, Fornaro, G., & Pauciullo, A., "Extension of 4-D SAR imaging to the monitoring of thermally dilating scatterers," *IEEE Trans. Geosci. Remote Sens.*, 51(12), 5296-5306, 2013

[63] K. Tomiyasu, "Conceptual performance of a satellite borne, wide swath synthetic aperture radar," *IEEE Trans. Geosci. Remote Sens.*, vol. 19, no. 2, pp. 108–116, Apr. 1981.

[64] G. Franceschetti and R. Lanari, Synthetic Aperture Radar Processing, Boca Raton, FL, USA: CRC,1999.

[65] Navarro CA, Hitschfeld-Kahler N, Mateu L. A Survey on Parallel Computing and its Applications in Data-Parallel Problems Using GPU Architectures. Communications in Computational Physics. 2014;15(2):285-329. doi:10.4208/cicp.110113.010813°

[66] W. J. Dally, S. W. Keckler and D. B. Kirk, "Evolution of the Graphics Processing Unit (GPU)," in IEEE Micro, vol. 41, no. 6, pp. 42-51, 1 Nov.-Dec. 2021, doi: 10.1109/MM.2021.3113475.

[67] C. Fu, Z. Wang and Y. Zhai, "A CPU-GPU Data Transfer Optimization Approach Based on Code Migration and Merging," 2017 16th International Symposium on Distributed Computing and Applications to Business, Engineering and Science (DCABES), Anyang, China, 2017, pp. 23-26, doi: 10.1109/DCABES.2017.13.

[68] N. Bianchessi and G. Righini, "Planning and scheduling algorithms for the COSMO-SkyMed constellation," Aerosp Sci Technol, vol. 12, no. 7, 2008, doi: 10.1016/j.ast.2008.01.001.

[69] Netlib Repository [online], Available: https://www.netlib.org

[70] G. Hager and G. Wellein, Introduction to High Performance Computing for Scientists and Engineers. Boca Raton, FL, USA: CRC Press, 2010.

[71] H. El-Rewini and M. Abd-El-Barr, Advanced Computer Architecture and Parallel Processing. Hoboken, NJ, USA: Wiley, 2005. doi: 10.1002/0471478385.

[72] L. D'Auria et al., "Magma injection beneath the urban area of Naples: A new mechanism for the 2012-2013 volcanic unrest at Campi Flegrei caldera," Sci Rep, vol. 5, 2015, doi: 10.1038/srep13100.

[73] F. Giudicepietro, Macedonio, G., & Martini, M. (2017). A physical model of sill expansion to explain the dynamics of unrest at calderas with application to Campi Flegrei. Frontiers in Earth Science, 5, 54.

[74] P. De Martino, Dolce, M., Brandi, G., Scarpato, G., Tammaro, U. (2021). The ground deformation history of the Neapolitan volcanic area (Campi Flegrei caldera, Somma-Vesuvius volcano, and Ischia Island) from 20 years of continuous GPS observations (2000-2019), Remote Sensing, 13:2725, doi:10.3390/rs13142725

[75] ASI, Italian Space Agency Upgrades Access To MAPITALY Data, [online] Available: https://www.asi.it/en/2023/12/asi-italian-space-agency-upgrades-access-to-mapitaly-data.

[76] M. Bonano, M. Manzo, F. Casu, M. Manunta, and R. Lanari, "DInSAR for the monitoring of cultural heritage sites", Sensing the Past (Geotechnologies and the Environment), N. Masini and F. Soldovieri, Eds. Cham, Switzerland: Springer, 2016, ch. 6, pp. 117–134, doi: 10.1007/978-3-319-50518-3_6.

[77] D A Talledo, A Miano, M Bonano, F Di Carlo, R Lanari, M Manunta, A Meda, A Mele, A Prota, A Saetta, A Stella, "Satellite radar interferometry: Potential and limitations for structural assessment and monitoring", Journal of Building Engineering 46, 103756, 2022, doi: 10.1016/j.jobe.2021.103756.

[78] D Festa, M Bonano, N Casagli, P Confuorto, C De Luca, M Del Soldato, R Lanari, P Lu, M Manunta, M Manzo, G Onorato, F Raspini, I Zinno, F Casu, "Nation-wide mapping and classification of ground deformation phenomena through the spatial clustering of P- SBAS InSAR measurements: Italy case study", ISPRS Journal of Photogrammetry and Remote Sensing 189, 1-22, 2022, doi: 10.1016/j.isprsjprs.2022.04.022.

[79] European Ground Motion Service [online]. Available: https://egms.land.copernicus.eu.

[80] INCREASE OF SENTINEL-1A ORBITAL TUBE: IMPACT ON INTERFEROMETRY [online], Available: https://sentinels.copernicus.eu/documents/d/sentinel/esa-eopg-eopgmq-tn-2024-12-increase-of-sentinel-1a-orbital-tube

[81] Geohazard Exploitation Platform [online]. Available: https://geohazards-tep.eu/#!

[82] Earthconsole platform [online]. Available:https://earthconsole.eu

[83] F. Delgado, T. Shreve, S. Borgstrom, P. León-Ibanez, J. Castillo and M. Poland, "A global assessment of SAOCOM-1 L-band stripmap data for InSAR characterization of volcanic, tectonic, cryospheric, and anthropogenic deformation," in IEEE Transactions on Geoscience and Remote Sensing, 2024, doi: 10.1109/TGRS.2024.3423792.

[84] Technical characteristics of the SAOCOM-1 system." Accessed: Jul. 08, 2022. [Online]. Available: https://www.argentina.gob.ar/ciencia/conae/misiones-espaciales/saocom/caracteristicas-tecnicas

[85] T. Motohka, Y. Kankaku, S. Miura and S. Suzuki, "Alos-4 L-Band SAR Mission and Observation," IGARSS 2019 - 2019 IEEE International Geoscience and Remote Sensing Symposium, Yokohama, Japan, 2019, pp. 5271-5273, doi: 10.1109/IGARSS.2019.8898169.

[86] K. Kellogg et al., "NASA-ISRO Synthetic Aperture Radar (NISAR) Mission," 2020 IEEE Aerospace Conference, Big Sky, MT, USA, 2020, pp. 1-21, doi: 10.1109/AERO47225.2020.9172638.

[87] F. Cotugno, Berardino, P., Bonano, M., et val., Constellation Design and Analysis for Spaceborne DInSAR Mapping in Mid Inclination Orbits: the IRIDE NIMBUS Mission. TechRxiv. May 20, 2024. DOI: 10.36227/techrxiv.171617381.15261636/v1